



Millimeter-Wave Reconfigurable Intelligent Surface With Independent and Continuous Amplitude-Phase Control: Unit Cell Design and Circuit Model

Downloaded from: <https://research.chalmers.se>, 2026-04-19 08:25 UTC

Citation for the original published paper (version of record):

Zhu, Y., Vilenskiy, A., Iupikov, O. et al (2025). Millimeter-Wave Reconfigurable Intelligent Surface With Independent and Continuous Amplitude-Phase Control: Unit Cell Design and Circuit Model. *IEEE Transactions on Antennas and Propagation*, 73(10): 7627-7641. <http://dx.doi.org/10.1109/TAP.2025.3577744>

N.B. When citing this work, cite the original published paper.

© 2025 IEEE. Personal use of this material is permitted. Permission from IEEE must be obtained for all other uses, in any current or future media, including reprinting/republishing this material for advertising or promotional purposes, or reuse of any copyrighted component of this work in other works.

Millimeter-Wave Reconfigurable Intelligent Surface With Independent and Continuous Amplitude-Phase Control: Unit Cell Design and Circuit Model

Yuqing Zhu, *Graduate Student Member, IEEE*, Artem Vilenskiy, *Senior Member, IEEE*, Oleg Iupikov, *Member, IEEE*, Pavlo Krasov, *Member, IEEE*, Thomas Emanuelsson, Gregor Lasser, *Senior Member, IEEE*, and Marianna Ivashina, *Senior Member, IEEE*

Abstract—This paper presents a reconfigurable intelligent surface (RIS) unit cell (UC) with independent amplitude-phase control, crucial for complex field shaping in RIS-assisted over-the-air testing. Unlike conventional phase-only tuning UCs, the proposed design enables continuous control from reflective to absorptive states for advanced field synthesis. To quantify reconfigurability, we introduce a generalized complex-plane representation, termed Γ -coverage, mapping both amplitude and phase over all bias states. For the first time at millimeter-wave frequencies, a loop-embedded end-folded UC integrating a forward-biased *p-i-n* diode and a reverse-biased varactor diode is developed to maximize Γ -coverage. The UC achieves a 0–0.5 amplitude tuning range (equivalent to a controllable loss from complete attenuation to 6 dB) and a -180° – $+180^\circ$ phase tuning range at 28 GHz. The maximum incident angle reaches 45° within $\pm 48^\circ$ phase fluctuations, extending to 60° with full-phase tuning under a 12 dB loss criterion. We derive empirical circuit models for both diodes to account for high-frequency parasitic effects and formulate a semi-analytical UC equivalent circuit model. The UC prototype is evaluated using a waveguide simulator. The operational bandwidths for reconfigurability are 25.8–28.0 GHz with a relative Γ -coverage area exceeding 25%, and 26.5–27.7 GHz for 360° phase control with 8.4–12 dB losses. The instantaneous bandwidth for stable operation spans 27.3–27.7 GHz, maintaining $\pm 50^\circ$ phase fluctuations within 5.6–13.4 dB losses. The UC is analyzed in an RIS-assisted near-field plane-wave generation scenario for a compact antenna test range (CATR), achieving high field uniformity (< 0.6 dB and $< 2.5^\circ$ errors). Despite intrinsic UC losses, the RIS-based CATR reduces total system loss by 22.8 dB compared to a far-field test range.

Index Terms—Equivalent circuit model, millimeter-wave, near field, over-the-air testing, reconfigurable intelligent surface.

I. INTRODUCTION

This research was conducted at the GigaHertz-ChaseOn Bridge Centre under the OTA5G+ project, funded by Rohde & Schwarz, Ericsson, Icomera, Bluetest, and Chalmers University of Technology. The paper revision was carried out within the Advanced Digitalization program at the WiTECH Centre under the AutoTA project, funded by Vinnova, Ericsson, Volvo Cars, RISE, Icomera, and UniqueSec. (*Corresponding author: Yuqing Zhu.*)

Y. Zhu, O. Iupikov, P. Krasov, and M. Ivashina are with the Antenna Systems Group, Department of Electrical Engineering, Chalmers University of Technology, 41296 Gothenburg, Sweden (e-mail: zhuyuqing@iee.org).

A. Vilenskiy was with the Antenna Systems Group, Department of Electrical Engineering, Chalmers University of Technology, 41296 Gothenburg, Sweden. He is now with Xpanceo, Dubai, UAE.

T. Emanuelsson is with Ericsson AB, 41756 Gothenburg, Sweden, and also with the Department of Microtechnology and Nanoscience, Chalmers University of Technology, 41296 Gothenburg, Sweden.

G. Lasser is with the Department of Microtechnology and Nanoscience, Chalmers University of Technology, 41296 Gothenburg, Sweden.

RECONFIGURABLE intelligent surfaces (RISs) have emerged as a transformative technology for future wireless communications by dynamically manipulating channel environments [1]. However, traditional RIS architectures (e.g., 1-bit or 2-bit phase-only control) are not optimal in near-field scenarios [2], where phase-only control cannot accurately shape the field distribution [3]. In applications such as RIS-assisted over-the-air (OTA) testing chambers, both the receiver and transmitter should preferably be located within the RIS near field. This configuration significantly reduces chamber size and enhances measurement dynamic range. Examples include a plane-wave (PW) generator that forms a confined test zone [4] and a wireless cable [5]. To meet accuracy demands of such configurations, RISs must support advanced field synthesis algorithms that utilize simultaneous amplitude-phase control across the reflection-absorption spectrum. This requires optimal RIS unit cell (UC) design with high-resolution biasing while accounting for amplitude-phase interdependence.

Despite extensive research on RISs with phase control [6], full amplitude-phase reconfigurability remains largely unexplored due to the substantially increased complexity [7]. UC designs for controlling both amplitude and phase are more commonly found in passive metasurfaces, which exploit diversity in UC size and type [8], angular orientation [9], or passive loading [10]. Nevertheless, these solutions are restricted to static applications [11], [12].

Recently, reflective RISs and reconfigurable metasurfaces with real-time, simultaneous amplitude-phase tuning have gained increasing attention. Several reconfigurable mechanisms have been investigated, including discrete diode films [13]–[20], graphene [21], [22], vanadium dioxide [23], and integrated circuits [24]. Among these, diode-integrated UCs are widely adopted due to their relatively low complexity and cost. For example, *p-i-n* diodes can be switched between ON and OFF states for 1-bit phase quantization [13] or biased in transition states for amplitude control [14], [15]. In these designs, amplitude and phase cannot be independently controlled, leading to a limited number of discrete UC states [16], [17]. Continuous amplitude-phase control can be achieved using two varactor diodes for arbitrary state combinations [18] or two separate coupled resonators [19]. However, both approaches suffer from a narrow amplitude-phase tuning range, thereby degrading control accuracy. While cascading programmable reflection-type attenuators and phase shifters

[20] enables full-phase coverage, the multi-layer topology with six diodes per UC presents a major limitation.

Furthermore, most reported amplitude-phase controllable UCs are limited to frequencies below 10 GHz, with their direct scalability to higher frequencies hindered by parasitic effects in existing tunable components [25], [26]. For instance, at K_a -band, off-the-shelf GaAs varactor diodes exhibit a narrow total capacitance tuning ratio (typically less than 1.8) [25], which poses difficulties in achieving a full phase range from -180° to $+180^\circ$. These challenges, along with the complexity of bias circuitry, have made multi-bit, phase-only tuning UCs rarely reported at millimeter-wave (mm-wave) frequencies, let alone UCs with both amplitude and phase control [27]–[29].

The scarcity of mm-wave designs also implies that existing modeling approaches remain largely unvalidated. While numerical electromagnetic (EM) simulation is the primary design tool, simpler physics-based models, like equivalent circuit models (ECMs), aid in understanding operating principles. However, current ECMs have reduced accuracy in predicting dependencies on frequency, incident angle, and configuration state [30]–[32]. Accuracy can be improved with explicit knowledge of the UC current distribution [33], which is typically available only for simple, regular geometries (e.g., dipoles and rectangular patches) [33]–[35]. Another challenge is the limited availability of circuit models for tunable electronics at mm-wave frequencies.

This paper presents the following contributions: (i) a generalized representation of UC reflection properties, termed Γ -coverage, which maps both amplitude and phase of Γ on the complex plane across a continuous range of bias states, along with performance metrics (A_{cov} and Γ_{max}) to quantify reconfigurability. This framework simplifies the analysis of independent amplitude-phase tuning and the selection of optimal bias states; (ii) the mm-wave UC design enabling independent and precise amplitude-phase control, suitable for RIS-assisted OTA testing as a near-field PW generator. The design incorporates critical diode parasitics and PCB-related losses through EM-circuit co-simulation that integrate numerical EM data with empirical data of diodes over all bias states; (iii) a semi-analytical UC ECM that combines Floquet modal expansion with lumped component modeling, enhancing accuracy across varying incident angles and validated for diode-loaded complex-shaped UC geometries.

The paper is organized as follows: Section II introduces the RIS UC and characterizes its tunable components. Section III describes the modeling approach and performance metrics. The ECM is established and validated in Section IV. Section V presents the experimental results, followed by a comparison with previous designs and a discussion of the targeted application in Section VI. Finally, Section VII concludes the paper.

II. AMPLITUDE-PHASE CONTROLLABLE RIS UNIT CELL

A. RIS UC Configuration

The proposed UC, shown in Fig. 1, features a square lattice of $0.42\lambda_0$, where λ_0 is the free-space wavelength at 28 GHz. It consists of two stacked dielectric substrates (Sub.1 and Sub.2) and four copper foil layers, bonded by a prepreg sheet. The

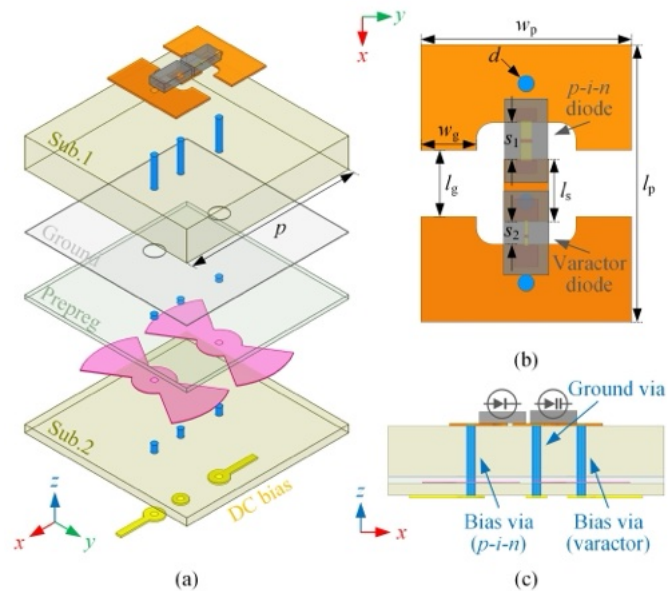


Fig. 1. Configuration of the mm-wave RIS UC featuring two vertical loops embedded within a segmented end-folded patch. A $p-i-n$ diode and a varactor diode are integrated on top, with DC bias lines applied at the bottom. (a) Exploded view. (b) Top view of the end-folded patch (on the upper metal layer). (c) Side view. Dimensions (in mm): $p = 4.5$, $l_p = 2.5$, $w_p = 1.9$, $l_g = 0.6$, $w_g = 0.5$, $l_s = 0.56$, $s_1 = 0.33$, $s_2 = 0.21$, and $d = 0.15$.

UC adopts a single-layer, diode-integrated scattering topology distributed on the grounded Sub.1, equipped with bias circuitry on Sub.2. Sub.1 and Sub.2 are 0.813-mm and 0.203-mm thick RO4003C laminates ($\epsilon_r = 3.55$, $\tan \delta = 0.0027$), respectively, while the prepreg is RO4450F ($\epsilon_r = 3.52$, $\tan \delta = 0.004$) with a thickness of 0.102 mm.

A segmented end-folded metal patch, printed on the top surface, provides reactive loading at the air-dielectric interface. A $p-i-n$ diode and a varactor diode bridge the gaps between patch segments. The $p-i-n$ diode functions as a current-controlled variable RC circuit in forward-biased states, while the varactor diode acts as a voltage-controlled variable capacitor in reverse-biased states. This combination allows independent amplitude-phase control across a broad tuning range, with both amplitude and phase responses determined by both diodes' bias states, as demonstrated in Section III. The two folded patch segments are symmetrical, with the shorter middle segment offset to accommodate the diodes. A ground plane on the bottom of Sub.1 isolates the patch from the bias circuitry on Sub.2.

Three plated through vias are embedded in the substrates to electrically connect the three segments. The addition of these vias transforms the planar patch topology into two vertical coupled loops while facilitating DC biasing of the diodes. The two bias vias are centrally positioned at the folded segments and connected to the radial stubs to function as RF chokes. The middle ground via is slightly off-center to symmetrize the current distribution, compensating for variations in diode parasitics. Both diodes are oriented with their cathodes facing the $+x$ -direction, requiring two positive voltages to be applied to the bottom DC bias lines for independent diode control.

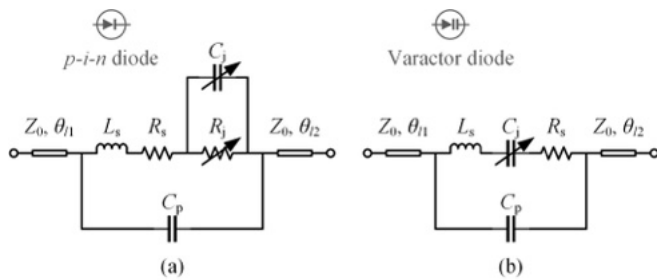


Fig. 2. Proposed circuit models of diodes. R_j and C_j are variable parameters representing the junction effects, while all others are fixed parameters. Anodes are on the left. (a) p - i - n diode. (b) Varactor diode.

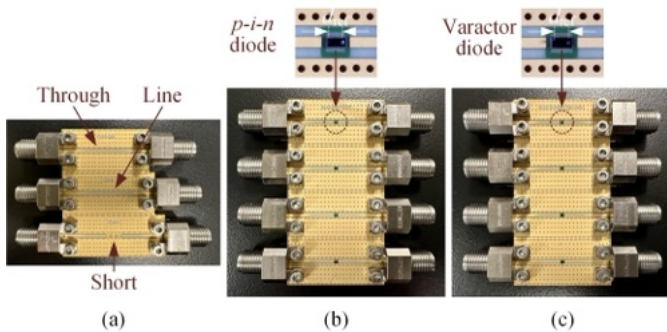


Fig. 3. Setup for diode characterization. Four identical diode samples are mounted on respective PCBs for repeated measurements. 2.92-mm clamp-on end-launch connectors are attached to both sides of each GCPW. The distance between the two measurement reference planes is $d_{\text{ref}} = 0.53$ mm. (a) TRL GCPW calibration kit. (b) p - i - n diodes. (c) Varactor diodes.

B. Characterization of p - i - n and Varactor Diodes

Diode modeling should account for parasitic effects at mm-wave frequencies and junction behaviors across continuous bias variations, especially for the p - i - n diode operating in OFF (zero voltage), ON (fully open junction), and transition states [36], rather than simple ON/OFF states for RF switching.

The proposed diode circuit models (DCMs) are depicted in Fig. 2. For the p - i - n diode, the junction effect is represented by a variable resistance R_j and a variable diffusion capacitance C_j in parallel, both controlled by the forward bias current I_f . This is an improved DCM that includes the carrier diffusion effect critical at mm-wave frequencies, as discussed in the authors' previous work [26]. For the varactor diode, the junction effect is represented by a variable capacitance C_j , controlled by the reverse bias voltage U_r . Note that the DCMs are de-embedded to the diodes' pads and thus include intrinsic diode parasitics, as well as pad- and substrate-related effects. This way, the models account for the intrinsic series inductance L_s and the contact resistance R_s ; the parallel capacitance C_p represents the cumulative effect of the diode packaging and edge pad capacitance. Two ideal transmission lines, with characteristic impedance Z_0 and electrical length θ_l , are added to the anode and cathode sides to reflect the time delay introduced by the physical length of the diodes and pads, which results in a non-negligible electrical length at mm-wave frequencies. Due to the asymmetry of the junction location, θ_{l1} and θ_{l2} are different.

Experimental characterization of diodes has been performed

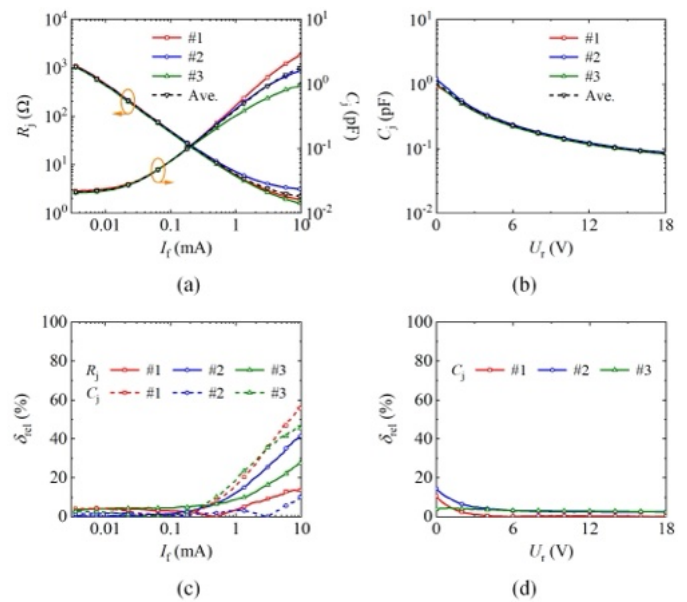


Fig. 4. Derived diode junction parameters as functions of DC biases, obtained by simulating the DCMs in ADS to fit the measured S -matrix of each diode. Results from three samples (#1–#3) are presented, with relative deviation from the average evaluated as δ_{rel} . (a) R_j and C_j of p - i - n diodes versus I_f . (b) C_j of varactor diodes versus U_r . (c) δ_{rel} of R_j and C_j . (d) δ_{rel} of C_j .

to verify the above DCMs, as shown in Fig. 3. In this study, we use the AlGaAs MADP-000907-14020W p - i - n diode and the GaAs MAVR-000120-14110G hyperabrupt varactor diode from MACOM. Both devices are flip-chip dies with a footprint of about 0.8×0.4 mm². The diodes are characterized in a 2-port configuration, inserted in series into 75 Ω grounded coplanar waveguides (GCPWs) on a RO4003C substrate. This impedance interface is chosen to match the GCPW signal line width with the diode width, thus minimizing parasitics caused by the line width step between the pads and GCPW. For each diode type, identical samples are used for repeated measurements to reduce uncertainty, with three well-welded, fully functional samples tested. An *ad hoc* through-reflect-line (TRL) calibration kit [Fig. 3(a)] is employed to shift the measurement reference planes to the diode pad edges (in each case, located $d_{\text{ref}}/2$ from the diode geometric center). Stepped DC forward and reverse biases (I_f or U_r) are applied through a bias tee of the VNA to measure S -parameters for all bias states from 20 GHz to 32 GHz.

The DCM parameters for both diodes are extracted by fitting the measured results. Fig. 4 shows the derived junction parameter curves. Other fixed parameters are listed in Table I. These empirical values are applicable to different frequencies, bias states, and diode samples. The procedure is as follows: First, circuit simulations of the established DCMs are performed in Keysight ADS, with the optimization objective as the measured entire S -matrix over 20–32 GHz, encompassing all bias states of each diode. Second, the S -matrix at individual bias states is utilized for parameter tuning, generating a set of fitting values for each fixed circuit parameter. Third, the fixed parameter values are selected as the average of these fitting values, as they remain constant across bias states. Fourth,

TABLE I
EXTRACTED FIXED EQUIVALENT PARAMETERS OF DIODES

Diodes	Z_0 (Ω)	θ_{l1} ($^\circ$)	θ_{l2} ($^\circ$)	L_s (nH)	R_s (Ω)	C_p (pF)
<i>p-i-n</i>	75	10.74	14.91	0.12	0.8	0.030
Varactor	75	12.18	16.70	0.08	1.8	0.038

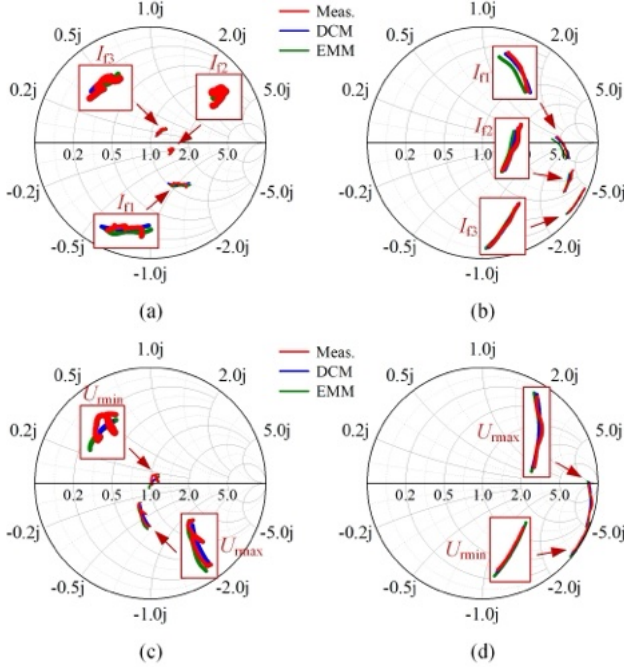


Fig. 5. S -parameters of *p-i-n* and varactor diodes on the Smith chart over 20–32 GHz from measurements, DCMs, and EMMs. Measurements are conducted with the GCPW-based setup, while DCMs and EMMs are simulated in ADS and HFSS, respectively. Several bias states are shown as examples. (a) S_{11} and (b) S_{21} of *p-i-n* diodes. (c) S_{11} and (d) S_{21} of varactor diodes. $I_{f1} = 0.02$ mA, $I_{f2} = 0.12$ mA, $I_{f3} = 2.31$ mA, $U_{r\min} = 0$ V, and $U_{r\max} = 18$ V.

this process is repeated for three samples, and the average results are reported in Table I. Finally, after determining the fixed parameters, the optimization is re-performed to obtain the junction parameters versus I_f or U_r for each sample, as plotted in Fig. 4(a) and Fig. 4(b). Here, the relative deviation δ_{rel} is introduced to assess consistency. It is calculated as the absolute difference in R_j or C_j between each sample and the average, normalized by the average to allow comparison across datasets with different scales or units. The results show that δ_{rel} is below 56% for *p-i-n* diodes and 14% for varactor diodes. The noticeable fluctuations at large I_f for *p-i-n* diodes are mainly due to temperature changes as the diodes heat up. For varactor and low- I_f *p-i-n* diodes, this effect is minor.

For exemplification, Fig. 5 presents circuit-level simulated and measured S -parameters at several bias states. Additionally, results from Ansys HFSS simulations of the 3D EM structures in Fig. 3, comprising the EM models (EMMs) of both diodes, are provided. Each EMM captures essential geometric details to model intrinsic diode parasitics; it also includes the diode pads. Junction effects are represented by the lumped RLC boundary with variable R_j or C_j , introduced differentially inside a gap on the diode signal line [Fig. 1(b)]. Such EMMs facilitate UC full-wave simulation by accounting for

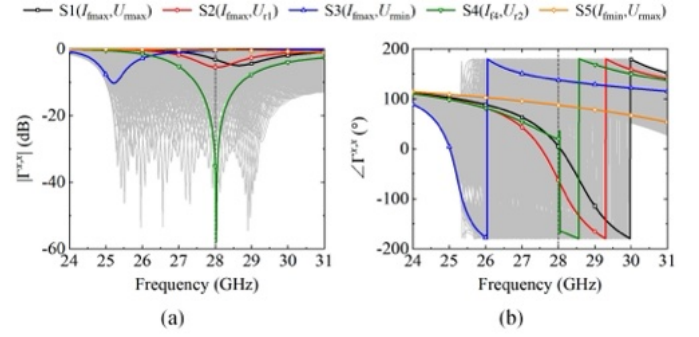


Fig. 6. Simulated Cartesian plots of $\Gamma^{x,x}$ versus frequency under normal PW incidence for all bias states (41×37 combinations of I_f and U_r), with five representative states (S1–S5) highlighted. $\Gamma^{x,x}$ is obtained from EM-circuit co-simulation in HFSS and ADS. (a) Amplitude. (b) Phase. $I_{f\min} = 5$ μ A, $I_{f\max} = 10$ mA, $I_{f4} = 0.33$ mA, $U_{r1} = 13.5$ V, and $U_{r2} = 11.5$ V.

coupling effects between the diode geometry and its external environment. The good agreement between simulations and measurements confirms the accuracy of these models.

III. MODELING AND ANALYSIS APPROACH

A. EM-Circuit Co-Simulation

Full-wave EM simulation is performed in Ansys HFSS with sidewall periodic boundaries and a Floquet port above the UC aperture. To reduce computational effort, a differential lumped port replaces the lumped RLC boundary in the EMM for circuit-level diode state switching. The latter is implemented in the Keysight ADS schematic environment by terminating the differential diode ports with varying junction impedance.

B. Γ -Coverage and Performance Metrics

A UC can be characterized by its reflection tensor Γ (an extension of the complex reflection coefficient Γ), which is a second-order affine tensor in 2D space. For a single linearly-polarized UC, it is convenient to express Γ in a basis aligned with the UC's characteristic axes, making the tensor structure weakly dependent on the incident angle (θ , φ). Consider the x -polarized case (as in the presented UC), we define Γ as

$$\Gamma = \begin{bmatrix} \Gamma^{x,x} & \Gamma^{x,y} \\ \Gamma^{y,x} & \Gamma^{y,y} \end{bmatrix} \quad (1)$$

where $\Gamma^{y,x}$ is the ratio of the y -component complex amplitude of the scattered wave to the x -component complex amplitude of the incident wave, and likewise for the others. For the x -polarized UC, $\Gamma^{x,x}$ is the controllable tensor element of interest, while $|\Gamma^{x,y}|$ and $|\Gamma^{y,x}|$ (which are responsible for cross-polarized reflections) are close to 0, and $|\Gamma^{y,y}|$ (indicating structural reflections related to the grounded dielectric slab) is close to 1. We note that in the Floquet EM analysis, the tensor elements are found in the “natural” TE-TM modal basis [37], which are then transformed into the x - y basis through the basis rotation matrix \mathbf{M} (derived in Section IV).

In this manner, Γ can be determined for each combination of I_f and U_r , as shown in the Cartesian plots of $\Gamma^{x,x}$ in Fig. 6. The total number of bias states is the product of

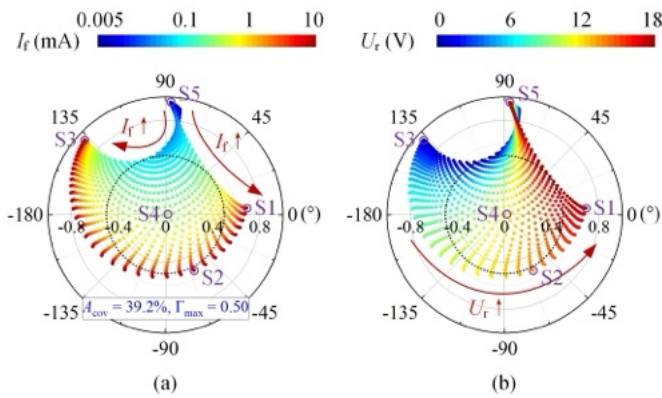


Fig. 7. Simulated Γ -coverage plots under normal PW incidence at 28 GHz, displaying $\Gamma^{x,x}$ for all bias states on the complex plane. $\Gamma^{x,x}$ is obtained from EM-circuit co-simulation in HFSS and ADS. The complex-plane representation can be transformed from the Cartesian plots in Fig. 6. The values of A_{cov} and Γ_{max} are calculated from Γ -coverage. S1–S5 are marked. The dot locations in (a) and (b) are identical, with color indicating (a) I_f and (b) U_r .

the sample counts for I_f and U_r , where I_f is set to increase from 5 μA to 10 mA in 41 logarithmically spaced samples, and U_r increases from 0 V to 18 V in 37 linearly spaced samples. However, since the Cartesian plots depict amplitude and phase separately, they fail to intuitively convey their interaction, obscuring the independence of amplitude-phase control. Moreover, the extensive range of bias states limits the Cartesian representation to qualitative observation.

To this end, we introduce a generalized representation, referred to as Γ -coverage, to visualize UC reflection properties by combining amplitude and phase information on the complex plane across all bias state combinations. For the $\Gamma^{x,x}$ component of interest, its coverage plot under normal PW incidence at 28 GHz is shown in Fig. 7. To simplify notation, we hereafter use Γ -coverage to denote $\Gamma^{x,x}$ -coverage. It describes a complex-plane region comprising all $\Gamma^{x,x}$ values, which can be transformed from the conventional Cartesian plot in Fig. 6 by specifying the target frequency. In contrast, this complex-plane representation explicitly links the simultaneous amplitude-phase response to each operating state (e.g., the highlighted states S1–S5) while also providing insights into the functionality of the p - i - n and varactor diodes. As shown, increasing I_f and U_r causes $\Gamma^{x,x}$ dots to move along curvilinear trajectories, instead of following a straight line through the origin or a perfect circular arc. While I_f predominantly affects the amplitude response and U_r predominantly affects the phase response, both I_f and U_r essentially exert concurrent influences on both amplitude and phase. Therefore, independent amplitude-phase control of the UC is achieved by selecting specific bias state combinations from Γ -coverage, rather than solely relying on independent diode biasing control.

Additionally, the proposed Γ -coverage provides a universal framework for evaluating reconfigurability. Two key performance metrics are defined to characterize the amplitude-phase controllable UC from distinct perspectives.

1) The relative area of Γ -coverage (denoted as A_{cov}). It refers to the ratio of the complex-plane Γ -coverage area (i.e., the colored region in Fig. 7) to the unit circle area (i.e., π).

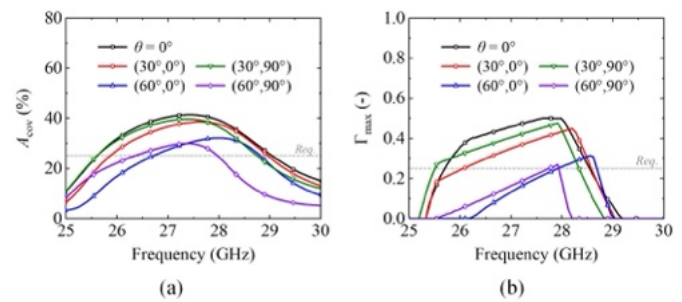


Fig. 8. Simulated A_{cov} and Γ_{max} versus frequency at incident angles (θ , φ). Parameter values are calculated from each Γ -coverage plot at different frequencies and incident angles. The requirements (req.) are defined as either $A_{\text{cov}} \geq 25\%$ or $\Gamma_{\text{max}} \geq 0.25$. (a) A_{cov} . (b) Γ_{max} .

It stands for the controllable proportion, measuring the UC's overall capability for amplitude and phase control.

2) The maximum amplitude of $\Gamma^{x,x}$ for -180° – $+180^\circ$ phase control (denoted as Γ_{max}). It refers to the radius of the maximum circle fully contained inside Γ -coverage (see the dotted circle in Fig. 7). Within this circular region, the UC enables full 360° phase control with an amplitude dynamic range from 0 to Γ_{max} . This region can also be expressed by its relative area, i.e., $\pi\Gamma_{\text{max}}^2/\pi 1^2 = \Gamma_{\text{max}}^2$.

Typically, Γ -coverage is irregular or non-circular, and thus $A_{\text{cov}} \geq \Gamma_{\text{max}}^2$. However, A_{cov} alone does not uniquely determine the distribution; a large A_{cov} may still correspond to a small Γ_{max} . Therefore, Γ_{max} is regarded as the primary metric of reconfigurability, while A_{cov} serves as a supportive metric that complements it by capturing the total spanned area.

The developed UC is intended for OTA testing applications [4], [5], where large Γ -coverage is desired. As shown in Fig. 7, Γ_{max} attains 0.5 (i.e., a minimum UC loss of 6 dB) at 28 GHz, with an A_{cov} of 39.2%. Simulations also reveal that $|\Gamma^{y,x}|$ is below -59 dB, $|\Gamma^{y,y}|$ is above -0.4 dB, and the coupling of the x -polarized incident wave to the DC bias lines is below -30 dB across the 24–31 GHz band and all bias states. Thus, these weak contributions are omitted from the analysis.

C. Operational and Instantaneous Bandwidths

The operational bandwidth is defined as the frequency interval where $A_{\text{cov}} \geq 25\%$ or $\Gamma_{\text{max}} \geq 0.25$. This is achieved by flexibly tuning the bias states at each frequency, indicating the UC's reconfigurability within a certain frequency range. Fig. 8 presents the frequency responses of A_{cov} and Γ_{max} . Under normal incidence, the simulated bandwidths are 25.6–29.0 GHz for $A_{\text{cov}} \geq 25\%$, and 25.7–28.6 GHz for $\Gamma_{\text{max}} \geq 0.25$. The UC is capable of operating up to $\theta = 60^\circ$, with both criteria satisfied around 28 GHz.

The instantaneous bandwidth is defined as the frequency interval where phase fluctuations remain within $\pm 50^\circ$ while the bias states are fixed. It quantifies the frequency stability of reflection properties under constant bias, potentially indicating the signal bandwidth the UC can manipulate. Fig. 9 shows the amplitude and phase of $\Gamma^{x,x}$ for thirteen states selected from Fig. 7. The black line at 28 GHz represents an ideal full-phase tuning range with 30° steps. Accordingly, the instantaneous

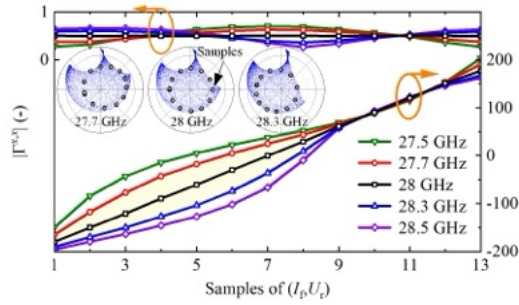


Fig. 9. Simulated amplitude and phase of $\Gamma^{x,x}$ versus bias states at several frequencies. Thirteen state samples (the black dots on the inset) uniformly distributed on the $\Gamma_{\max} = 0.5$ circle at 28 GHz are selected. The respective (I_b, U_b) values are (0.61, 8.2), (1.33, 10.0), (2.86, 11.3), (5.10, 12.5), (4.63, 13.6), (2.36, 14.9), (1.09, 16.4), (0.46, 17.8), (0.16, 15.9), (0.06, 5.3), (0.09, 0.8), (0.26, 5.5), and (0.56, 8.0), all in (mA, V).

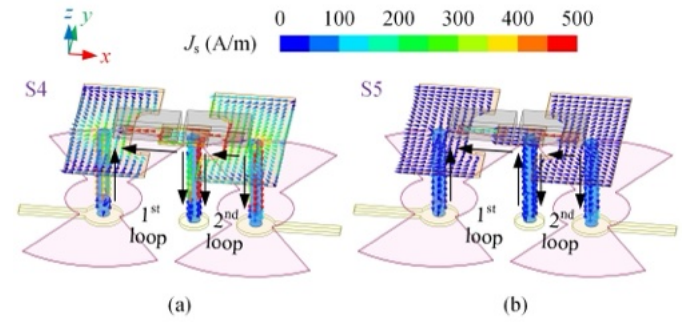


Fig. 11. Simulated current distributions at 28 GHz for different bias states: (a) S4 with almost-full absorption; (b) S5 with almost-full reflection. J_s denotes surface current density. The phase delay is set to 330° in simulation for clearer observation and fair comparison. The current on the patch is shown on its lower surface. The ground plane and substrates are hidden for clarity.

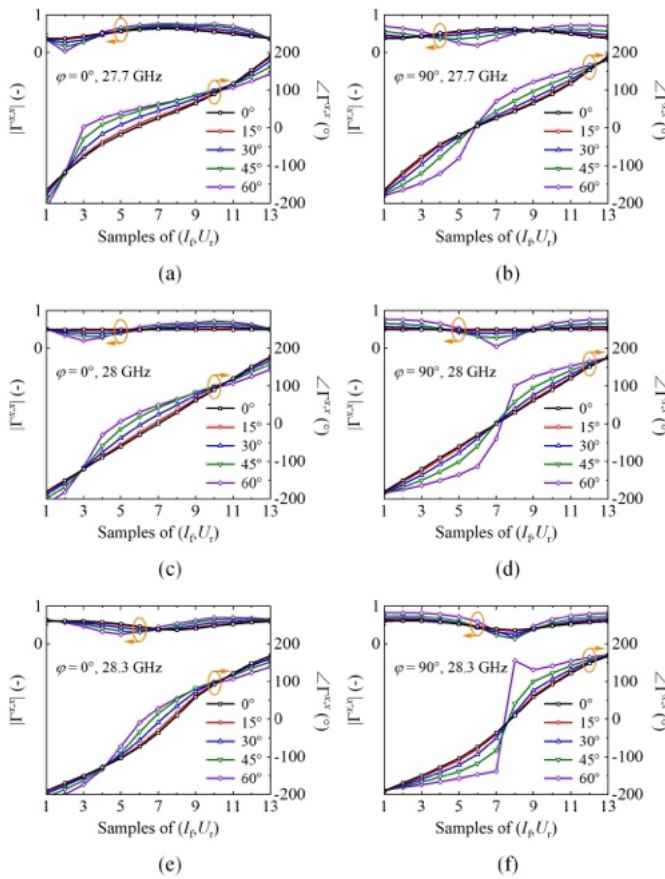


Fig. 10. Simulated amplitude and phase of $\Gamma^{x,x}$ versus bias states at incident angles (θ, φ) . The thirteen state samples remain the same as those in Fig. 9. (a) $\varphi = 0^\circ$ and (b) $\varphi = 90^\circ$ at 27.7 GHz. (c) $\varphi = 0^\circ$ and (d) $\varphi = 90^\circ$ at 28 GHz. (e) $\varphi = 0^\circ$ and (f) $\varphi = 90^\circ$ at 28.3 GHz.

bandwidth spans 27.7–28.3 GHz (the yellow shaded area). The oblique incidence case, analyzed in Fig. 10, demonstrates stability up to $\theta = 45^\circ$, with phase fluctuations within $\pm 48^\circ$ at 28 GHz and $\pm 52^\circ$ across the instantaneous bandwidth.

D. Interpretation of Γ -coverage in the Design Process

To illustrate the UC operating mechanism, Fig. 11 shows surface current distributions for the bias states leading to

almost-full absorption (S4) and reflection (S5), as seen from the Γ -coverage in Fig. 7. The via-loaded patch forms two adjacent loops that support vertical currents. Due to the extended folded segments, currents are further distributed along the patch edges. Thus, mutual coupling occurs between the loops and between the folded ends. For S4, incomplete conduction in the p - i - n diode weakens current intensity on the first loop. For S5, currents concentrate at the diode junctions due to their narrower width. The current flow remains consistent across states, though the current direction of the ground via may change as a result of the superposition of surface and displacement currents from the two loops.

Fig. 12 presents a parametric study of the UC alongside its key geometric evolution. Each UC's Γ -coverage is evaluated at its optimal operating frequency—defined by the peak Γ_{\max} —to highlight performance potential. Corresponding A_{cov} and Γ_{\max} curves are also shown to illustrate frequency-dependent behavior. The starting point, UC 1, features a planar dipole topology with p - i - n and varactor diodes, optimized for amplitude-phase control at 28 GHz based on a half-wavelength resonance. However, the realized control range is limited, and the UC 1 dimensions are already comparable to the diode sizes, restricting design flexibility. To address this, UC 2 extends the lateral segment lengths on both sides, increasing the patch's capacitance and expanding Γ -coverage. This modification, however, inevitably lowers the optimal operating frequency of the fundamental mode to 21.7 GHz. Building upon this, UC 3 incorporates three vias to form two coupled loops. The vertical currents in these loops significantly modify the original patch mode, restoring the frequency to the desired value by virtue of the vias' shunt inductance effect [38], while simultaneously enabling independent diode biasing. Although A_{cov} improves, the Γ_{\max} circle noticeably shrinks due to the downward-shifted Γ -coverage and reduced phase tuning range, resulting from the altered UC impedance. To mitigate this, UC 4 introduces folded ends to enhance inter-segment coupling capacitance, thereby maximizing Γ -coverage while minimizing the frequency shift. The electrically compact nature of the metal pattern is preserved, retaining the same longitudinal length as UC 1. The complex current magnitudes at the almost-full absorption state confirm the observed via

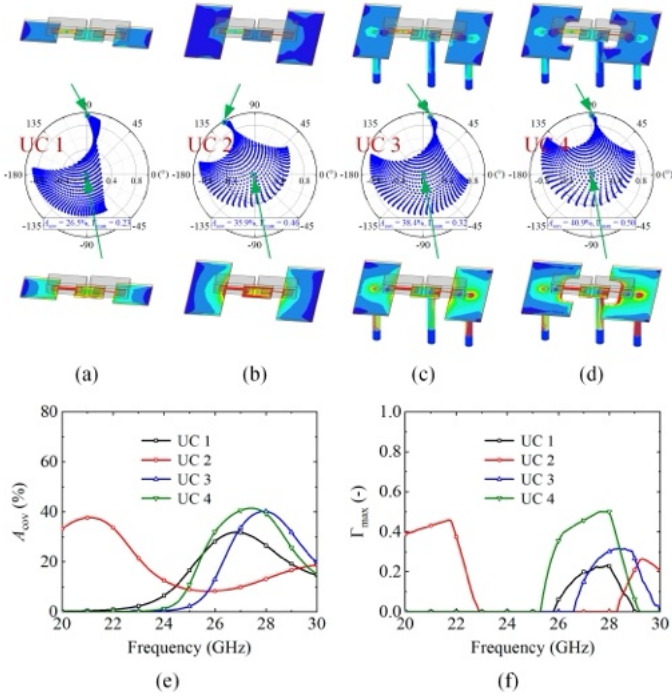


Fig. 12. Parametric study of the UC, including the dipole-type UC 1, the UC 2 with extended segments, the unfolded UC 3 with vias and bias circuitry, and the proposed UC 4. All other structures and parameters remain consistent. (a)–(d) Simulated Γ -coverage plots of the four UCs, visualizing the complex current magnitudes at the almost-full absorption and reflection states, using the same scale as in Fig. 11. The results are shown at their respective optimal operating frequencies where Γ_{\max} is maximized, i.e., 28 GHz, 21.7 GHz, 28.4 GHz, and 27.7 GHz. (e), (f) Simulated A_{cov} and Γ_{\max} versus frequency.

and diode effects in Fig. 11. At the almost-full reflection state, current distributions across UCs are similar, with the dominant contribution originating from the ground plane.

IV. EQUIVALENT CIRCUIT MODEL

A. Semi-Analytical ECM of the UC

The ECM development begins with Floquet mode analysis in an infinite array, involving the modal source decomposition of TE_{mn} and TM_{mn} types (w.r.t. the z -axis). Analogous to driven-mode phased arrays, the input admittance for a given Floquet excitation mode ($m = m_0$ and $n = n_0$) in a general scattering RIS can be derived as shown in [33], [34]

$$Y_{\text{in},mn}^{\text{TE|TM}} = Y_{mn}^{\text{TE|TM}'} T_{mn}^{\text{TE|TM}} + Y_{\text{sub},mn}^{\text{TE|TM}} \quad (2)$$

where the first term represents the equivalent surface admittance at the air-dielectric interface ($z = 0$) for this excitation mode. It is expressed as the admittance $Y_{mn}^{\text{TE|TM}'}$, contributed by all other Floquet modes ($m \neq m_0$ or $n \neq n_0$) and tunable components (i.e., diodes in this context), scaled by a transformation factor $T_{mn}^{\text{TE|TM}}$ for the mode of interest. The second term, $Y_{\text{sub},mn}^{\text{TE|TM}}$, represents the input admittance of the grounded dielectric slab, in parallel with the former. Typically, m_0 and n_0 are set to 0 for the dominant Floquet modes.

Inspired by this formulation, the proposed ECM is shown in Fig. 13, where the TE_{00} or TM_{00} mode is considered for the UC. The input admittance in (2) is mapped to this ECM.

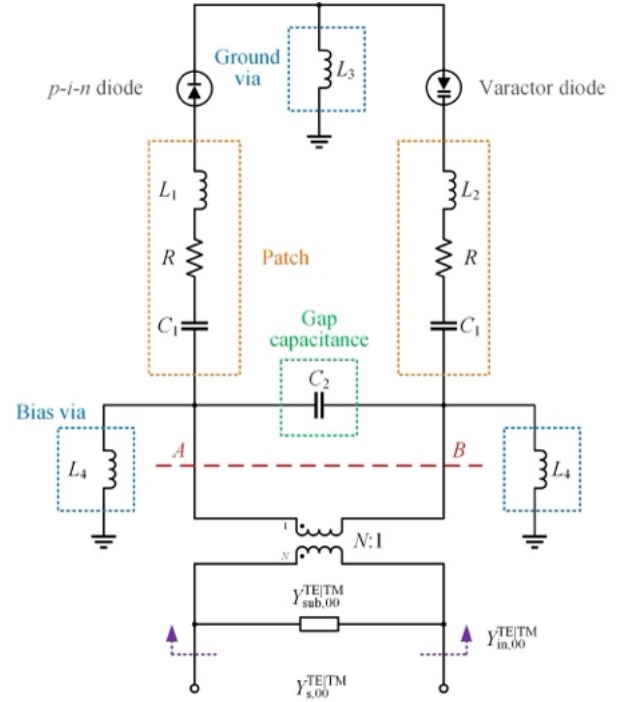


Fig. 13. Schematic of the UC ECM, formulated using a semi-analytical approach combining Floquet modal expansion and lumped component modeling, with DCMs as building blocks. The final parameter values, optimized in ADS, are $N = 2.71$, $L_1 = 0.45$ nH, $L_2 = 0.30$ nH, $L_3 = 0.38$ nH, $L_4 = 0.43$ nH, $R = 1.14$ Ω , $C_1 = 0.052$ pF, and $C_2 = 0.057$ pF.

Specifically, at $z = 0$, $Y_{mn}^{\text{TE|TM}'}$ refers to the admittance seen upward from line \overline{AB} , while $T_{mn}^{\text{TE|TM}}$ is physically interpreted as a transformer with turns ratio N [33], [34]; that is,

$$N = \sqrt{T_{mn}^{\text{TE|TM}}}. \quad (3)$$

In addition, the ECM contains an input port for an incident PW in the $z > 0$ region with wave admittance $Y_{s,mn}^{\text{TE|TM}}$. In the $z < 0$ region, the grounded dielectric slab is regarded as a short-circuited transmission line with electrical length h and input admittance $Y_{\text{sub},mn}^{\text{TE|TM}}$. These quantities are given by [37]

$$Y_{s,mn}^{\text{TE|TM}} = Y_{mn}^{\text{TE+|TM+}} \quad (4)$$

$$Y_{\text{sub},mn}^{\text{TE|TM}} = -jY_{mn}^{\text{TE-|TM-}} \cot(k_{zmn}^- h). \quad (5)$$

The modal admittances are [37]

$$Y_{mn}^{\text{TE+}} = \frac{k_{zmn}^+}{\omega\mu_0}, Y_{mn}^{\text{TE-}} = \frac{k_{zmn}^-}{\omega\mu_0} \quad (6)$$

$$Y_{mn}^{\text{TM+}} = \frac{\omega\varepsilon_0}{k_{zmn}^+}, Y_{mn}^{\text{TM-}} = \frac{\omega\varepsilon_0\varepsilon_r}{k_{zmn}^-} \quad (7)$$

where the wave numbers along the z -axis are

$$k_{zmn}^+ = \sqrt{k_0^2 - k_{xmn}^2 - k_{ymn}^2} \quad (8)$$

$$k_{zmn}^- = \sqrt{(\varepsilon_r - j\varepsilon_r \tan \delta) k_0^2 - k_{xmn}^2 - k_{ymn}^2} \quad (9)$$

with the Floquet wave numbers

$$k_{xmn} = k_{x0} + \frac{2m\pi}{p}, k_{ymn} = k_{y0} + \frac{2n\pi}{p}. \quad (10)$$

Here, the Floquet transverse wave numbers k_{x0} and k_{y0} depend on the incident angle (θ, φ) [37], which are

$$k_{x0} = k_0 \sin \theta \cos \varphi, \quad k_{y0} = k_0 \sin \theta \sin \varphi. \quad (11)$$

The above formulas provide an analytical solution to the ECM via Floquet modal expansion. For the part above line \overline{AB} , it should be replaced by $Y_{mn}^{\text{TE}'|\text{TM}'}$, which however directly relies on the UC's current distribution. While a closed-form solution for current distribution exists for regular UC geometries, it does not apply to generalized UCs with complex configurations. Therefore, a more suitable alternative is to establish a lumped *RLC* equivalent model.

Based on the diode characterization, the DCMs from Section II serve as building blocks for the ECM. Both diodes are connected to the patch in the orientation shown in Fig. 1, dividing it into two major end-folded segments, with each segment modeled as an *RLC* series resonant circuit. Due to differences in diode pad dimensions, the side connected to the *p-i-n* diode has a slightly longer current path, leading to the constraint $L_1 > L_2$. Since both segments are equal in size and symmetrically positioned relative to the UC boundary, the same capacitance C_1 is used to represent their charge storage capability and the mutual capacitance between adjacent UCs. The resistance R stands for ohmic loss.

Following Fig. 11, three inductances with a common ground are introduced to represent the contributions of the vertical currents supported by the ground and bias vias, denoted as L_3 and L_4 . They correspond to the self partial inductance of the cylindrical wire segment [39]. L_3 is placed between the diodes, while L_4 lies outside the *RLC* series circuit. Since the ground via is terminated by the ground plane, whereas the bias vias extend to the radial stubs, the additional constraint $L_3 < L_4$ must hold. The radial stubs act as large distributed capacitances, allowing the bias vias to be treated as short-circuited at mm-wave frequencies, thus forming two closed loops. As discussed in Section III, the folded ends of the patch enhance coupling between the segments. This structure represents a discontinuity in the microstrip transmission line, forming a foreshortened open circuit and a series gap ($l_g \times w_g$), modeled as a gap capacitance C_g [40]. In the UC, two identical coupled gaps are arranged in parallel, yielding $C_2 = 2C_g$.

Finally, upon obtaining the input admittance in (2), the scalar co-polarized reflection coefficient is described by [41]

$$\Gamma_{mn}^{\text{TE}|\text{TM}} = \frac{Y_{s,mn}^{\text{TE}|\text{TM}} - Y_{in,mn}^{\text{TE}|\text{TM}}}{Y_{s,mn}^{\text{TE}|\text{TM}} + Y_{in,mn}^{\text{TE}|\text{TM}}}. \quad (12)$$

Note that both EM and ECM analyses employ Floquet field decomposition; thus, the reflection tensor is constructed in the TE-TM modal basis. Similar to Γ in (1), we define

$$\Gamma' = \begin{bmatrix} \Gamma^{\text{TE,TE}} & \Gamma^{\text{TE,TM}} \\ \Gamma^{\text{TM,TE}} & \Gamma^{\text{TM,TM}} \end{bmatrix}. \quad (13)$$

Hence, the result in (12) corresponds to one of the diagonal elements in Γ' (depending on φ), i.e., $\Gamma^{\text{TE,TE}}$ or $\Gamma^{\text{TM,TM}}$. A further step is needed to express Γ' in the x - y basis to eliminate the φ -dependence and align the polarizations. This requires a spatial transformation to the Cartesian coordinate system,

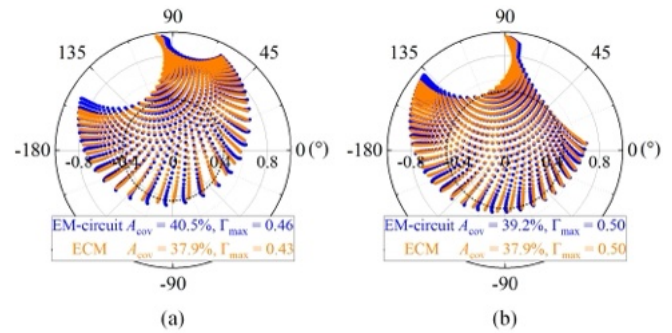


Fig. 14. Simulated Γ -coverage plots under normal PW incidence, comparing two simulation methods. Blue dots are from EM-circuit co-simulation in HFSS and ADS, and orange dots are from simulating the ECM in ADS. Γ_{\max} circles correspond to ECM results. (a) 27 GHz. (b) 28 GHz.

reverting to (1). We have derived that it is an orthogonal similarity transformation, given by

$$\Gamma = \mathbf{M}^{-1} \Gamma' \mathbf{M} = \mathbf{M}^T \Gamma' \mathbf{M} \quad (14)$$

where the entries of the transformation matrix \mathbf{M} are $M_{11} = \sin \varphi$, $M_{12} = -\cos \varphi$, $M_{21} = \cos \varphi$, and $M_{22} = \sin \varphi$.

The combination of Floquet modal expansion with lumped component numerical/empirical modeling completes the proposed ECM. This semi-analytical approach calculates exact solutions for partial terms, while utilizing empirical values for quantities like partial inductance and gap capacitance as starting points. Small margins (up to 50%) are allowed for refinement to match full-wave simulation results under normal incidence. This results in a coherent ECM tailored for RF scenarios, enhancing the understanding of operating principles.

B. Performance under Normal and Oblique Incidence

To verify the ECM, circuit simulations are performed in Keysight ADS. The theoretical part is inherently incorporated by explicitly entering the quantities defined in (4)–(11) into the ADS schematic, following the circuit framework implied by (2) and (3). Upon specifying the incident angle for TE or TM excitations, the reflection coefficient is computed using (12) and then transformed into the x - y basis via (13) and (14). The bias ranges and step sizes for I_f and U_r are identical to those in EM-circuit co-simulations to ensure a fair comparison. First, Γ -coverage under normal incidence is evaluated using both methods, as shown in Fig. 14. At 27 GHz and 28 GHz, nearly point-to-point consistency is observed, with negligible differences in A_{cov} and Γ_{\max} . Fig. 15 shows the Γ -coverage plots under oblique incidence at 28 GHz. The Γ -coverage from both methods agrees well at $\theta = 30^\circ$ in both azimuthal planes. As θ increases to 60° , noticeable differences appear in the $\varphi = 0^\circ$ plane (E-plane), particularly in the upper-right rotation. However, in the $\varphi = 90^\circ$ plane (H-plane), the ECM remains a good match. The differences at large incident angles between the $\varphi = 0^\circ$ and $\varphi = 90^\circ$ planes are mainly due to the x -polarized UC geometry without rotational symmetry.

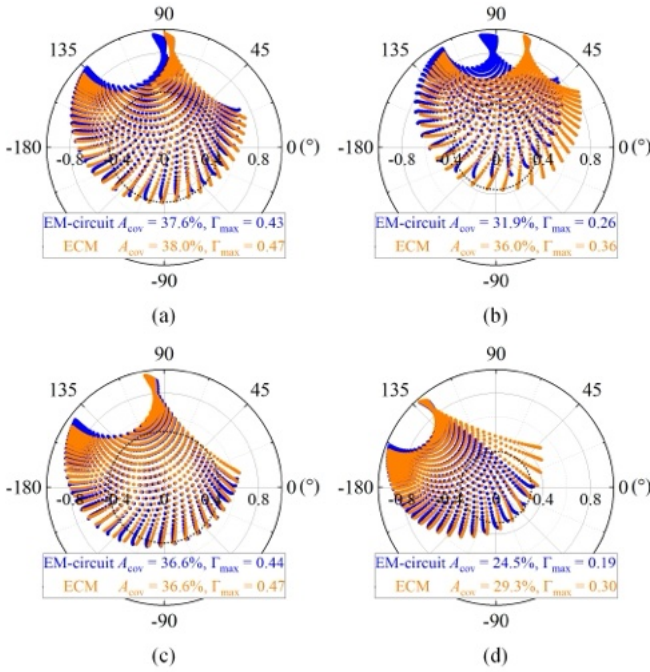


Fig. 15. Simulated Γ -coverage plots under oblique PW incidence at 28 GHz, comparing two simulation methods. Blue dots are from EM-circuit co-simulation in HFSS and ADS, and orange dots are from simulating the ECM in ADS. Γ_{\max} circles correspond to ECM results. (a) $\theta = 30^\circ$ and (b) $\theta = 60^\circ$ in the $\varphi = 0^\circ$ plane. (c) $\theta = 30^\circ$ and (d) $\theta = 60^\circ$ in the $\varphi = 90^\circ$ plane.

For Floquet modes with wave numbers k_{xmn} and k_{ymn} , the resonant UC is more susceptible to k_{xmn} . To analyze this, we compute the ratio of k_{xmn} to k_0 as

$$\frac{k_{xmn}}{k_0} = \sin \theta \cos \varphi + \frac{2m\pi}{k_0 p} = \sin \theta \cos \varphi + \frac{\lambda_0 m}{p} \quad (15)$$

where $\lambda_0/p = 2.38$ for the selected UC period. In two planes,

$$\left. \frac{k_{xmn}}{k_0} \right|_{\varphi=0^\circ} = \sin \theta + 2.38m, \quad \left. \frac{k_{xmn}}{k_0} \right|_{\varphi=90^\circ} = 2.38m. \quad (16)$$

As expected, k_{xmn} varies with θ only in the $\varphi = 0^\circ$ plane, indicating that the UC performance in this plane is more prone to change. The extent of this effect becomes evident as θ increases, especially when p is relatively large. For smaller UC lattices, the proportion of the $\sin \theta$ term in (16) is minor.

From another perspective, the placement of the three vias in the UC also contributes to this difference. As the vias are aligned along the $\varphi = 0^\circ$ plane, they interact electrically with the oblique incident TM wave in this plane but remain invisible to the TE wave in the $\varphi = 90^\circ$ plane. This effect should be reflected in the inductances L_3 and L_4 . Typically, the UC current distribution varies with the incident angle, meaning all equivalent parameters in the ECM should be θ -dependent. In the established ECM, these lumped quantities remain fixed to facilitate versatility and ease of application, which is effective as long as the angular sensitivity of the UC is sufficiently low.

The A_{cov} distributions from both EM-circuit co-simulation and ECM simulation are presented in Fig. 16. The similarity is higher in the $\varphi = 90^\circ$ plane than in the $\varphi = 0^\circ$ plane. However, for $\theta \leq 40^\circ$, the results in the $\varphi = 0^\circ$ plane remain

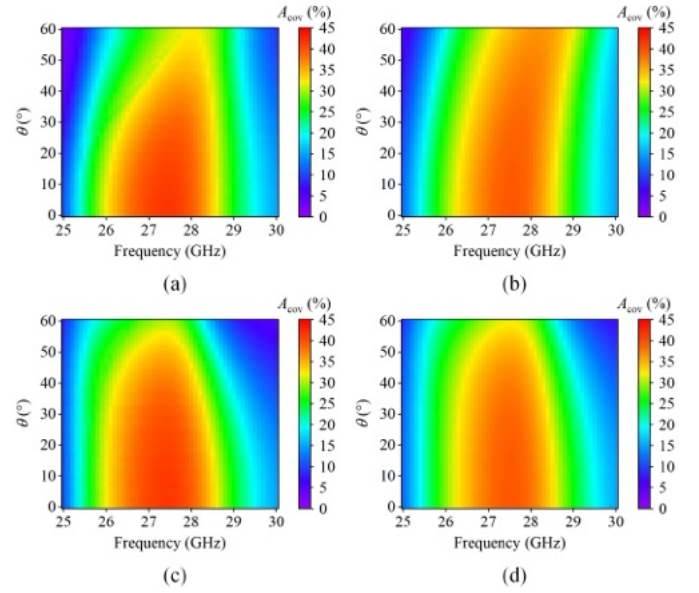


Fig. 16. Simulated A_{cov} distributions versus incident angle and frequency, comparing results from EM-circuit co-simulation and ECM simulation. (a) EM-circuit and (b) ECM results in the $\varphi = 0^\circ$ plane. (c) EM-circuit and (d) ECM results in the $\varphi = 90^\circ$ plane.

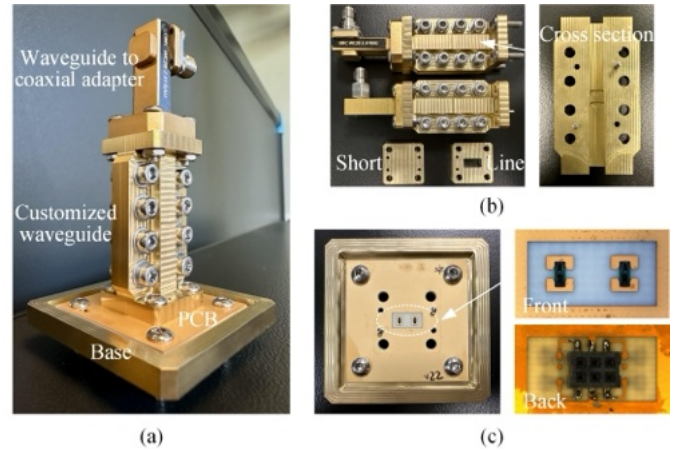


Fig. 17. Setup for UC characterization with a waveguide simulator, emulating an infinite RIS under varying oblique incidence at different frequencies. DC cables connected from the bottom are omitted for clarity. (a) Waveguide simulator. (b) TRL waveguide calibration kit. (c) PCB with 1×2 UCs.

nearly identical, with deviations appearing beyond this range. Therefore, the proposed ECM can be regarded as valid for $\theta \in [-40^\circ, 40^\circ]$ in the $\varphi = 0^\circ$ plane and $\theta \in [-60^\circ, 60^\circ]$ in the $\varphi = 90^\circ$ plane within 25–30 GHz.

V. EXPERIMENTS WITH THE WAVEGUIDE SIMULATOR

A. Experimental Setup

So far, the UC has been analyzed in an infinite RIS using both EM and circuit approaches. This section employs a well-established waveguide simulator technique for cost-effective experimental validation. Based on image theory, the waveguide emulates an infinite array for the UC and provides quasi-PW excitation to examine its scattering characteristics [42].

Fig. 17 shows the prototypes. The brass waveguide components are CNC-machined. The 1×2 UCs are placed side by side and attached to one end of the customized waveguide, with an aperture dimension equal to the size of the two UCs. The other end is converted to a standard WR-28 waveguide via an internal quarter-wavelength impedance transformer, thereby connected to a waveguide-to-coaxial adapter for measurement purposes. A TRL calibration kit consisting of back-to-back 2-port waveguides is used as the measurement reference at the waveguide interfaces. The waveguide is assembled from two identical blocks along the E-plane, using press-fit and slip-fit dowel pins for precise alignment and secure fixation. A milled metal base holds the PCB, preventing bending and ensuring structural stability. To simulate electric walls, the peripheral outline of the two UCs is enclosed by two fences of plated through vias. These vias are filled and capped during PCB manufacturing, rendering them invisible under a microscope. The diodes are manually soldered to the UCs, while the bias lines are routed from the backside and soldered to a surface-mounted six-position 1.0-mm-pitch socket for DC cable connections. Biasing is provided by digital-to-analog converters (DAC81416) from Texas Instruments, which output a 0–20 V buffered voltage with 16-bit resolution. Additional voltage-to-current converters are cascaded with the DACs for p - i - n diodes. Therefore, continuous control is implemented with 16-bit resolution for both amplitude and phase.

In this setup, the UC is excited under a specific oblique incidence for each frequency [42], namely at $\varphi = 90^\circ$ and

$$\theta = \arccos \left[\sqrt{1 - (\lambda_0/\lambda_c)^2} \right] \quad (17)$$

where $\lambda_c = 4p$ is the cut-off wavelength of the TE₁₀ mode.

B. Γ -coverage, Operational, and Instantaneous Bandwidths

Fig. 18 shows the measured Γ -coverage at various frequencies, alongside simulated results from waveguide-excited UCs. The measurements use the same bias settings as in previous simulations. The $\Gamma^{x,x}$ dot distributions in both results exhibit good agreement, with consistent rotational trends across frequencies, except for minor deviations at higher frequencies. Fig. 19 presents the frequency responses of A_{cov} and Γ_{max} . Simulated results from an infinite RIS at equivalent oblique angles, calculated using (17), are also provided. The measured operational bandwidths are 25.8–28.0 GHz for $A_{\text{cov}} \geq 25\%$, and 26.5–27.7 GHz for $\Gamma_{\text{max}} \geq 0.25$. The measured maximum values are 34.1% for A_{cov} at 27 GHz and 0.38 for Γ_{max} at 27.5 GHz. The measured results validate the predicted trends for both A_{cov} and Γ_{max} , with a 350 MHz frequency shift in the waveguide simulator closely aligning with simulations.

In comparison, the measured A_{cov} and Γ_{max} are smaller than the simulated ones, as reflected by the lower outline of the Γ -coverage plots in Fig. 18, indicating potential higher loss in the UC structure and measurement uncertainties. These discrepancies will be discussed in the following sub-section.

The measured amplitude and phase of $\Gamma^{x,x}$ are shown in Fig. 20 for frequency stability analysis. The bias states are selected from the measured Γ_{max} circle [Fig. 18(c)], following

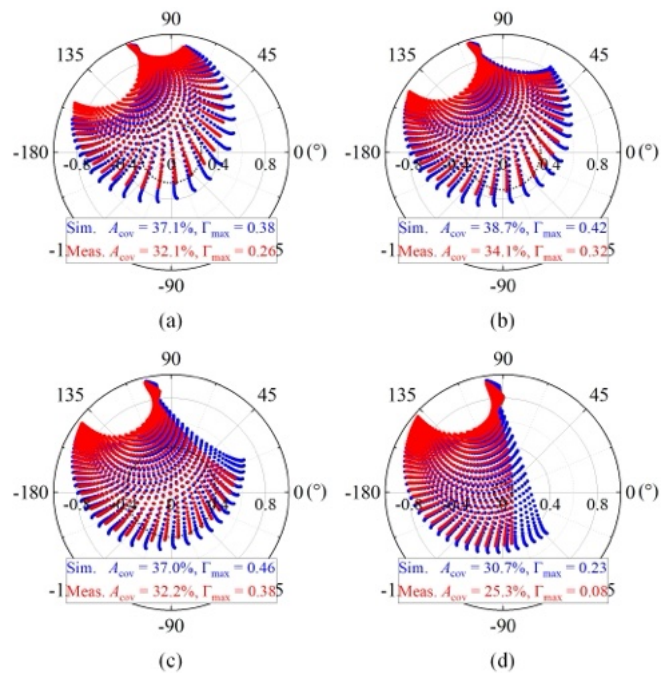


Fig. 18. Simulated (blue dots) and measured (red dots) Γ -coverage plots with the waveguide simulator. Simulated results are from EM-circuit co-simulation in HFSS and ADS, with a customized waveguide exciting the two UCs. Measurements are taken with the waveguide setup. Γ_{max} circles correspond to measured results. (a) 26.5 GHz. (b) 27 GHz. (c) 27.5 GHz. (d) 28 GHz.

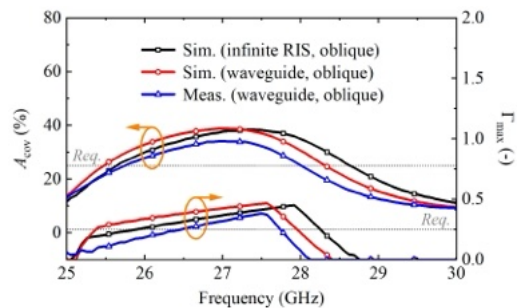


Fig. 19. Simulated and measured A_{cov} and Γ_{max} versus frequency. Parameter values are calculated from each Γ -coverage plot from EM-circuit co-simulations (in both infinite and waveguide environments) and measurements. The requirements (req.) are defined as either $A_{\text{cov}} \geq 25\%$ or $\Gamma_{\text{max}} \geq 0.25$.

a similar approach as in Fig. 9. The measured instantaneous bandwidth, defined by $\pm 50^\circ$ phase fluctuations, is 27.3–27.7 GHz (400 MHz). The phase curves match waveguide-based simulations at these states, with a small frequency shift.

C. UC Loss Analysis

A series of experiments has been conducted to identify potential sources of additional measured losses. First, the surface roughness of the copper foil is found to be critical for the UC. Based on Rogers laminate specifications and passive UC measurements (without diode loading), the Huray surface roughness model with a nodule radius of $0.7 \mu\text{m}$ and a surface ratio of 4 is applied in full-wave simulations. However, this non-ideal feature may still be underestimated. Second, materials used for diode mounting show a visible impact.

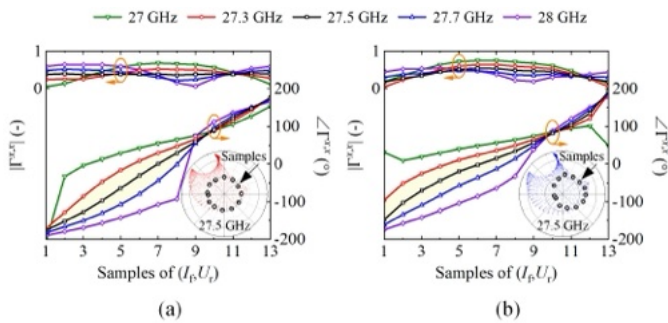


Fig. 20. Measured and simulated amplitude and phase of $\Gamma^{x,x}$ versus bias states at several frequencies. Thirteen state samples (the black dots on the inset) uniformly distributed on the $\Gamma_{\max} = 0.38$ circle measured at 27.5 GHz are selected. The respective (I_r, U_r) values are (0.58, 10.5), (1.24, 11.5), (2.19, 12.5), (5.65, 13.5), (10.00, 14.5), (5.65, 15.5), (2.19, 16.5), (0.85, 17.0), (0.40, 17.0), (0.19, 14.0), (0.15, 9.5), (0.22, 8.5), and (0.48, 10.0), all in (mA, V). (a) Measured results. (b) Simulated results.

Specifically, mounting with conductive adhesive causes about 4.5 dB more loss in Γ_{\max} than solder paste. However, manual soldering uncertainty introduces only minimal variation, as confirmed by multiple PCB samples. Third, a measurement comparison of fabricated UCs with two different PCB surface finishes—electroless nickel immersion gold (ENIG) and electroless palladium immersion gold (EPIG)—reveals that ENIG introduces 1.2 dB more loss than EPIG. Additional potential loss sources include air gaps in the structural assembly and processing tolerances. Common dielectric and ohmic losses, as well as diode parasitic effects, are already incorporated into the detailed UC and diode modeling. At mm-wave frequencies, these factors become increasingly significant, collectively contributing to the total reflection loss of the UC.

The UC loss is further detailed in Table II. The Γ -coverage confirms that the UC can operate in either reflective or absorptive mode with controllable losses, where low loss is preferred for reflection and high loss for absorption. For the reflection criterion ensuring a full -180° – $+180^\circ$ phase range (C1.2), the minimum loss is 6 dB under normal incidence and 8.4 dB under oblique incidence (experimentally measured). This trade-off in UC loss enables a wide tuning range (i.e., 0 – Γ_{\max} for amplitude and -180° – $+180^\circ$ for phase) while maintaining high accuracy (nearly continuous control with 16-bit resolution for both amplitude and phase). Additionally, lower losses can be achieved at specific phase points (C1.1). Losses are also evaluated over both the operational and instantaneous bandwidths (C1.3 and C1.4). For the absorption criterion, near-infinite losses can be generated at the desired frequency through high-precision biasing (C2.1), with losses exceeding 14.2 dB over the instantaneous bandwidth (C2.2).

VI. COMPARISON AND DISCUSSION

A. UC Comparison

A UC-level performance comparison between the proposed design and previous works is summarized in Table III. While several designs demonstrate electrical reconfigurability of amplitude-phase responses, most are constrained to discrete 1-bit phase quantization [13], [14], or provide only a limited

number of switching states for both amplitude and phase [15], [17]. Moreover, their control capabilities are restricted, as UCs share DC bias lines along a column, preventing independent control [13]–[15], [17]. The UC in [20] enables continuous amplitude and full-phase control; however, it suffers from a complex multi-layer configuration, with significantly higher diode counts and cost. Additionally, these implementations primarily operate below 10 GHz. While some recently developed UCs have started exploring mm-wave frequencies, they still fall into the category of 1-bit or 2-bit phase-only control [28], [29]. In contrast, the proposed UC addresses these limitations with simultaneous, independent, and continuous amplitude-phase control, and is demonstrated at mm-wave frequencies for the first time. The UC loss, when compared to [20], highlights the challenges of mm-wave implementation, particularly since the operating frequency in this work is approximately seven times higher. Furthermore, this study establishes a physically consistent ECM, accounting for critical diode parasitic effects and increased loss at mm-wave frequencies.

B. RIS-Assisted OTA Testing Application: PW Generator

Despite the reflection loss associated with Γ_{\max} potentially hindering efficiency, the design holds substantial promise for broader applications where this factor is less critical, especially in OTA testing of wireless devices. Unlike typical wireless communications, where SNR (and thus loss) is crucial, the RIS in this context synthesizes a reconfigurable channel matrix to enable dynamic test environments for devices under test (DUTs), serving as a cost-effective alternative to large-scale mm-wave active phased arrays and compact antenna test ranges (CATRs). Herein, RIS-induced losses are no longer a major concern, as inherent system losses can be calibrated and compensated during testing. The main drawback is a marginal reduction in the available dynamic range of the measurement setup, expressed as the difference between the maximum measurable signal and the minimum detectable signal above the noise floor. Consequently, the proposed UC is well-suited for OTA testing applications, where precise amplitude-phase control (e.g., at least 4-bit [4] or 5-bit [5] resolution for both parameters) is essential, while loss and efficiency requirements are of secondary importance and can be relaxed.

To demonstrate, the UC is analyzed in an RIS-assisted near-field PW generation scenario, similar to a reflect/transmitarray-based CATR [43], [44], but enabling tunable PW arrival angles without mechanical rotation. This scenario is simulated using the methodology in [4], with an RIS model comprising 21×21 UCs. A 9 dBi pyramidal horn is used as the feed, and an 11×11 bow-tie array with 22.8 dBi gain serves as the DUT. The RIS, illuminated by the feed, aims to generate a PW that minimizes amplitude-phase errors (< 1 dB and $< 10^\circ$) within a confined test zone. An optimal field synthesis algorithm [4] is applied to the UCs to ensure the required field uniformity. Fig. 21 shows the simulated setup, emphasizing the necessity of diverse UC states, ranging from almost-full absorption (see UCs at the RIS edges with $|\Gamma^{x,x}| < -20$ dB) to high reflection (see UCs around the RIS center with $|\Gamma^{x,x}| \approx -6$ dB). The feed-RIS and RIS-DUT distances are

TABLE II
UC LOSS BASED ON REFLECTION AND ABSORPTION CRITERIA

Reflection criterion (C1.1–C1.4)	UC loss (dB)	Frequency (GHz)	Angle (°)	Bias state (mA, V)	Comment
C1.1: Minimum loss at an individual phase point	0.4	28	$\theta = 0$	S5: $I_f = 0.005, U_f = 18$	Sim., infinite RIS
	0.4	27.5	$\theta = 37.3$	$I_f = 0.005, U_f = 18$	Mea., waveguide
C1.2: Minimum loss over the 360° phase range	6.0	28	$\theta = 0$	(I_f, U_f) for $\Gamma_{\max} = 0.5$	Sim., infinite RIS
	8.4	27.5	$\theta = 37.3$	(I_f, U_f) for $\Gamma_{\max} = 0.38$	Mea., waveguide
C1.3: Loss over the operational bandwidth	6–12	25.7–28.6	$\theta = 0$	(I_f, U_f) for $\Gamma_{\max} \geq 0.25$	Sim., infinite RIS
	8.4–12	26.5–27.7	$\theta = 37.0\text{--}39.0$	(I_f, U_f) for $\Gamma_{\max} \geq 0.25$	Mea., waveguide
C1.4: Loss over the instantaneous bandwidth	4–8.8	27.7–28.3	$\theta = 0$	(I_f, U_f) for $\Gamma_{\max} = 0.5$ at 28 GHz	Sim., infinite RIS
	2.7–17.6	27.7–28.3	$\theta = 45$	(I_f, U_f) for $\Gamma_{\max} = 0.5$ at 28 GHz	Sim., infinite RIS
	5.6–13.4	27.3–27.7	$\theta = 37.0\text{--}37.6$	(I_f, U_f) for $\Gamma_{\max} = 0.38$ at 27.5 GHz	Mea., waveguide
Absorption criterion (C2.1–C2.2)	UC loss (dB)	Frequency (GHz)	Angle (°)	Bias state (mA, V)	Comment
C2.1: Maximum achievable loss	∞	28	$\theta = 0$	S4: $I_f = 0.33, U_f = 11.5$	Sim., infinite RIS
	∞	27.5	$\theta = 37.3$	$I_f = 0.58, U_f = 13.5$	Mea., waveguide
C2.2: Loss over the instantaneous bandwidth	14.2– ∞	27.7–28.3	$\theta = 0$	S4: $I_f = 0.33, U_f = 11.5$	Sim., infinite RIS
	15.4– ∞	27.3–27.7	$\theta = 37.0\text{--}37.6$	$I_f = 0.58, U_f = 13.5$	Mea., waveguide

TABLE III
UC-LEVEL COMPARISON WITH PREVIOUS WORKS

Reference	[13]	[14]	[15]	[17]	[20]	[28]	[29]	This work
Design frequency (GHz)	7.85	10	3	4.9	4.15	27.5	26.1	28
Amplitude control (-)	0.45–0.92*	0.1–0.9	0.2, 0.6, 0.85*	0.4, 0.85	0.13–0.71	No	No	0–0.5* 0–0.38#
Phase control (°)	–120, 60	90, 290	0, 90, 180, 270	0, 45, 90, 135, 180, 225, 270, 315	0–426	–360, –180	–125.6, –32.9, 50.7, 148.5	–180–+180
Actual bits of amplitude & phase	N/A & 1-bit	N/A & 1-bit	N/A & 2-bit	1-bit & 3-bit	16-bit & 16-bit	0 & 1-bit	0 & 2-bit	16-bit & 16-bit
Configuration	Trapezoidal patch	Rectangular strip	Patch & strip	Stacked patch & mesh	Rectangular & E-patch	Patch & circular cutout	Segmented patch	Vertical loop & end-folded patch
Tunable component	2 <i>p-i-n</i> diodes	1 <i>p-i-n</i> diode	1 <i>p-i-n</i> & 1 varactor diode	2 varactor diodes	2 <i>p-i-n</i> & 4 varactor diodes	1 <i>p-i-n</i> diode	2 <i>p-i-n</i> diodes	1 <i>p-i-n</i> & 1 varactor diode
Suitable for independent UC control	No	No	No	No	Yes	Yes	Yes	Yes
Substrate layer	1	1	1	2	4	2	3	2
Periodicity (λ_0)	0.42	0.33	0.10, 0.18	0.33	0.42	0.35	0.44	0.42
Thickness (λ_0)	0.05	0.10	0.03	0.08	0.10	0.17	0.14	0.10
Minimum loss (dB) & criterion	0.7 for 1-bit phase control	0.9 for 1-bit phase control	1.4 for 2-bit phase control	1.4 for 3-bit phase control	3.0 for full phase control	2.8 ^{†1} for 1-bit phase control	1.9 ^{†2} for 2-bit phase control	6.0 for full phase control
Operational bandwidth (GHz) & definition	N/A	N/A	N/A	N/A	4.1–4.3 (4.8%) Definition not specified	N/A	N/A	25.6–29 (12.5%) for $A_{\text{cov}} \geq 25\%$; 25.7–28.6 (10.7%) for $\Gamma_{\max} \geq 0.25$
Instantaneous bandwidth (GHz) & definition	7.8–8.15 (4.4%) for a phase difference of $180^\circ \pm 37^\circ$	N/A	N/A	N/A	N/A	22.7–30.5 (29.3%) for a phase difference of $180^\circ \pm 20^\circ$	25.4–27 (6.1%) for a phase standard deviation $< 32.5^\circ$	27.7–28.3 (2.1%) for a $\pm 50^\circ$ phase fluctuation
ECM	Not validated	Not validated	Not validated	Yes	No	No	No	Yes
UC experimental characterization	Bistatic extraction from the RIS panel	Monostatic extraction from the RIS panel	No UC measurement	Bistatic extraction from the RIS panel	Bistatic extraction from the RIS panel	No UC measurement	Bistatic extraction from the RIS panel	Waveguide simulator with 1×2 UCs

N/A: Not available in the referenced context.

* Simulated under normal incidence at their respective design frequencies.

Measured under equivalent oblique incidence ($\theta = 37.3^\circ, \varphi = 90^\circ$) at 27.5 GHz using the waveguide simulator.

† For the phase-only control case, the UC loss is reported as the maximum value, either ^{†1} within the UC operating band or ^{†2} at the design frequency.

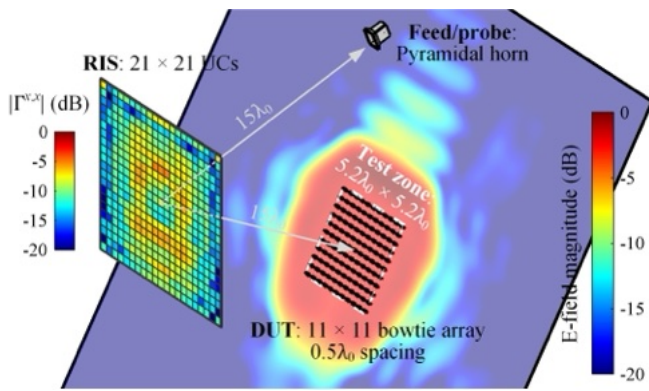


Fig. 21. Simulated setup for RIS-assisted near-field PW generation at 28 GHz, where the UCs' color codes represent the amplitude of $\Gamma^{x,z}$. The simulation model accounts for inter-element mutual coupling effects in the RIS and the DUT array, while assuming negligible edge truncation/diffraction and multi-scattering effects with the horn. The RIS semi-subtended angle is about 20° .

TABLE IV
RIS-BASED CATR AND EQUIVALENT FAR-FIELD SETUP

Measurement setup	Phase error ($^\circ$)	Distance* (λ_0)	Loss (dB)
RIS-CATR (ideal UC)	1.7	15 / 15	20.4 [#]
Far-field setup w/o RIS	1.7	1475	53.5 [†]
RIS-CATR (presented UC)	2.5	15 / 15	27.6 [#]
Far-field setup w/o RIS	2.5	991	50.4 [†]
Far-field setup w/o RIS	22.5 [§]	109	30.8 [†]

* For the RIS-CATR setup, the feed-RIS and RIS-DUT distances are shown; for the far-field setup, the distance required to achieve the same phase error as in the RIS-CATR setup is provided.

[#] Obtained via simulation of the transmission coefficient (i.e., coupling) between the feed and the DUT.

[†] Free-space path loss calculated using the Friis transmission formula.

[§] $\pi/8$ rad, typically used for far-field definition.

relatively short (both $15\lambda_0 \approx 0.16$ m), while the E-field amplitude and phase errors across the DUT aperture remain below 0.6 dB and 2.5° , respectively. In contrast, an equivalent far-field setup achieving the same phase uniformity would require a much larger distance between the probe (i.e., the horn without RIS) and the DUT—about 10.62 m ($991\lambda_0$)—leading to significantly higher total signal loss. Table IV compares the PW generator with far-field setups for both an ideal UC (lossless, supporting unit-circle Γ -coverage with full amplitude-phase tunability) and the practical UC in this study. The proposed UC contributes 7.2 dB to the system loss compared to an ideal UC, but achieves a 22.8 dB reduction relative to a far-field test range. Therefore, the practical UC losses have minimal impact on the considerably enhanced dynamic range of the RIS-enabled CATR.

Fig. 22 illustrates the operational bandwidth of the RIS-assisted PW generator, defined by amplitude errors below 1 dB and phase errors below 10° within the synthesized test zone. As shown, the achieved bandwidth is 25.5–28.5 GHz (3 GHz), attributed to the UCs' ability to adjust their optimal Γ values with frequency. However, if a single-frequency beamformer is applied and held fixed across the band, the instantaneous signal bandwidth of the setup is expected to be limited—about 70 MHz in this case. Therefore, it is customary to employ

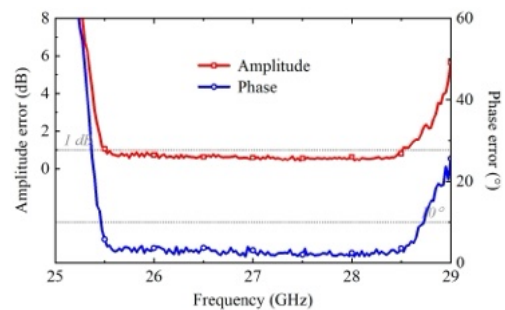


Fig. 22. Simulated PW E-field amplitude and phase errors versus frequency within the synthesized test zone, generated by the RIS-assisted PW generator using a 21×21 RIS panel composed of the proposed UC. Uniform PW formation is optimized at each frequency, with performance criteria of amplitude error < 1 dB and phase error $< 10^\circ$.

multi-frequency optimization in PW generators, which can increase the instantaneous bandwidth by a factor of 4 to 8 (see Fig. 11 in [45]), depending on the RIS panel size.

VII. CONCLUSION

We report the first development and validation of an amplitude-phase tunable RIS UC at mm-wave frequencies, essential for emerging near-field applications such as RIS-assisted OTA testing. To assess the reconfiguration range and continuity—ideally from full absorption to full reflection with multiple states—we introduce Γ -coverage, a generalized representation of reflection properties, along with the relative Γ -coverage area A_{cov} and the maximum amplitude Γ_{max} for 360° phase control. The UC is realized as a two-loop end-folded structure with a p - i - n diode and a varactor diode, enabling independent and continuous amplitude-phase control. The inductive loops interact with the variable diode impedance, supporting diverse reflection/absorption states while allowing independent biasing. The end-folded design enhances reconfigurability by extending Γ -coverage. Circuit models for both diodes and the UC are formulated and verified across the frequency band, all bias states, and varying incident angles.

The UC achieves a full phase tuning range and an amplitude tuning range of 0–0.5 (simulated under normal incidence at 28 GHz) and 0–0.38 (measured under oblique incidence at 27.5 GHz). The corresponding minimum UC losses of 6 dB ($\Gamma_{\text{max}} = 0.5$) and 8.4 dB ($\Gamma_{\text{max}} = 0.38$) highlight the necessary trade-offs in maximizing amplitude-phase tuning. The UC's measured 400 MHz instantaneous bandwidth aligns with the channel bandwidth specified for the 5G mm-wave FR2 spectrum [46], supporting a variety of in-band measurements.

The UC is exemplified as an RIS-assisted near-field PW generator for a CATR. Despite intrinsic UC losses, the RIS-based CATR improves the measurement system's dynamic range by 22.8 dB at 28 GHz compared to an equivalent far-field test range with the same 2.5° phase errors, owing to the shorter feed-RIS-DUT distances. This representative example substantiates the UC's potential for OTA testing applications.

ACKNOWLEDGMENT

The authors would like to thank Heinz Mellein, Benoit Derat (Rohde & Schwarz, Germany), and Jonas Friden, Christos

Kolitsidas (Ericsson, Sweden) for the fruitful discussions.

REFERENCES

- [1] M. Di Renzo, A. Zappone, M. Debbah, M.-S. Alouini, C. Yuen, J. de Rosny, and S. Tretyakov, "Smart radio environments empowered by reconfigurable intelligent surfaces: How it works, state of research, and the road ahead," *IEEE J. Sel. Areas Commun.*, vol. 38, no. 11, pp. 2450–2525, Nov. 2020.
- [2] Y. Jiang, F. Gao, M. Jian, S. Zhang, and W. Zhang, "Reconfigurable intelligent surface for near field communications: Beamforming and sensing," *IEEE Trans. Wireless Commun.*, vol. 22, no. 5, pp. 3447–3459, May 2023.
- [3] A. Tabeshnezhad, Y. Zhu, A. Vilenskiy, L. V. Nguyen, A. L. Swindlehurst, and T. Svensson, "Jammer mitigation in absorptive RIS-assisted uplink NOMA," *arXiv:2408.16786*, Aug. 2024.
- [4] O. A. Iupikov, A. R. Vilenskiy, Y. Zhu, P. S. Krasov, and M. V. Ivashina, "Reconfigurable intelligent surfaces for OTA testing: Optimization and initial results," in *Proc. IEEE Conf. Antenna Meas. Appl. (CAMA)*, Genoa, Italy, Nov. 2023, pp. 846–851.
- [5] P. S. Krasov, O. A. Iupikov, A. R. Vilenskiy, Y. Zhu, and M. V. Ivashina, "Reconfigurable intelligent surfaces for OTA testing: Wireless cable" in *Proc. 54th Eur. Microw. Conf. (EuMC)*, Paris, France, Sep. 2024, pp. 232–235.
- [6] Y. Feng, Q. Hu, K. Qu, W. Yang, Y. Zheng, and K. Chen, "Reconfigurable intelligent surfaces: Design, implementation, and practical demonstration," *Electromagn. Sci.*, vol. 1, no. 2, pp. 1–21, Jun. 2023.
- [7] Y. Saifullah, Y. He, A. Boag, G.-M. Yang, and F. Xu, "Recent progress in reconfigurable and intelligent metasurfaces: A comprehensive review of tuning mechanisms, hardware designs, and applications," *Adv. Sci.*, vol. 9, no. 33, Art. no. 2203747, Nov. 2022.
- [8] T. Y. Chen, Y. B. Li, H. Li, H. P. Wang, J. L. Shen, and T. J. Cui, "Arbitrary power allocation for multiple beams using amplitude- and phase-coded metasurfaces," *J. Phys. D, Appl. Phys.*, vol. 54, no. 16, Art. no. 165106, Apr. 2021.
- [9] L. Bao, R. Y. Wu, X. Fu, Q. Ma, G. D. Bai, J. Mu, R. Jiang, T. J. Cui, "Multi-beam forming and controls by metasurface with phase and amplitude modulations," *IEEE Trans. Antennas Propag.*, vol. 67, no. 10, pp. 6680–6685, Oct. 2019.
- [10] M. K. Emara, D. Kundu, K. Macdonell, L. M. Rufail, and S. Gupta, "Coupled resonator-based metasurface reflector with enhanced magnitude and phase coverage," *IEEE Trans. Antennas Propag.*, vol. 72, no. 1, pp. 901–914, Jan. 2024.
- [11] W.-L. Guo, K. Chen, G.-M. Wang, X.-Y. Luo, T. Cai, C.-B. Zhang, Y. Feng, "Airy beam generation: Approaching ideal efficiency and ultra wideband with reflective and transmissive metasurfaces," *Adv. Opt. Mater.*, vol. 8, no. 21, Art. no. 2000860, Nov. 2020.
- [12] H. Wang, Y. Cheng, L. Huang, Y. Li, H. Bai, R. Zhao, Q. Wei, W. Wan, H. Chen, J. Zhang, and S. Qu, "Simultaneous control of amplitude and phase via shifting isotropy to anisotropy for achieving holographic metamirror," *Opt. Exp.*, vol. 29, no. 26, pp. 43745–43756, Dec. 2021.
- [13] J. Liao, S. Guo, L. Yuan, C. Ji, C. Huang, and X. Luo, "Independent manipulation of reflection amplitude and phase by a single-layer reconfigurable metasurface," *Adv. Opt. Mater.*, vol. 10, no. 4, Art. no. 2101551, Feb. 2022.
- [14] H. L. Wang, Y. K. Zhang, T. Y. Zhang, H. F. Ma, and T. J. Cui, "Broadband and programmable amplitude-phase-joint-coding information metasurface," *ACS Appl. Mater. & Interfaces*, vol. 14, no. 25, pp. 29431–29440, Jun. 2022.
- [15] J. C. Liang, L. Zhang, Z. W. Cheng, P. Zhang, and T. J. Cui, "Flexible beam manipulations by reconfigurable intelligent surface with independent control of amplitude and phase," *Front. Mater.*, vol. 9, Art. no. 946163, Jul. 2022.
- [16] H. P. Wang, Y. B. Li, H. Li, J. L. Shen, S. Y. Dong, S. Y. Wang, K. N. Qi, Q. Ma, S. Jin, S. J. Li, and T. J. Cui, "Intelligent metasurface with frequency recognition for adaptive manipulation of electromagnetic wave," *Nanophotonics*, vol. 11, no. 7, pp. 1401–1411, 2022.
- [17] Q. Xiong, Z. Zhang, X. Ma, C. Huang, M. Pu, J. Luo, Y. Guo, Y. Wang, W. Bai, J. Ye, L. Yan, and X. Luo, "Multi-channel wireless communication based on amplitude-phase reconfigurable space-coding beamforming metasurface," *Adv. Electron. Mater.*, vol. 10, no. 8, Art. no. 2400056, Aug. 2024.
- [18] R. Phon, M. Lee, C. Lor, and S. Lim, "Multifunctional reflective metasurface to independently and simultaneously control amplitude and phase with frequency tunability," *Adv. Opt. Mater.*, vol. 11, no. 14, Art. no. 2202943, Jul. 2023.
- [19] M. K. Emara, D. Kundu, K. Macdonell, L. M. Rufail, and S. Gupta, "Dynamic metasurface reflectors based on coupled resonators for simultaneous magnitude and phase control," *IEEE Access*, vol. 11, pp. 129552–129565, 2023.
- [20] Y. H. Liu, S. Y. Wang, K. N. Qi, and Y. B. Li, "Dynamic controlling the bistatic RCS by programmable metasurface with continuous and independent manipulation of reflective phase and amplitude," *IEEE Antennas Wireless Propag. Lett.*, vol. 23, no. 3, pp. 1000–1004, Mar. 2024.
- [21] J. Zhang, X. Wei, I. D. Rukhlenko, H.-T. Chen, and W. Zhu, "Electrically tunable metasurface with independent frequency and amplitude modulations," *ACS Photon.*, vol. 7, no. 1, pp. 265–271, Dec. 2019.
- [22] C. Huang, J. Liao, C. Ji, J. Peng, L. Yuan, and X. Luo, "Graphene-integrated reconfigurable metasurface for independent manipulation of reflection magnitude and phase," *Adv. Opt. Mater.*, vol. 9, no. 7, Art. no. 2001950, Apr. 2021.
- [23] J. Shabanpour, S. Beyraghi, and C. R. Simovski, "THz multiple-beam manipulation by reconfigurable intelligent surface with independent phase/amplitude control," in *Proc. 17th Int. Congr. Artif. Mater. Novel Wave Phenomena*, Chania, Greece, Sep. 2023, pp. 338–340.
- [24] K. M. Kossifos, J. Georgiou, and M. A. Antoniadis, "ASIC-enabled programmable metasurfaces—Part 1: Design and characterization," *IEEE Trans. Antennas Propag.*, vol. 72, no. 3, pp. 2790–2799, Mar. 2024.
- [25] Y. Zhu, A. R. Vilenskiy, O. A. Iupikov, P. S. Krasov, T. Emanuelsson, G. Lasser, and M. V. Ivashina, "A varactor-based reconfigurable intelligent surface concept for 5G/6G mm-wave applications," in *Proc. 18th Eur. Conf. Antennas Propag. (EuCAP)*, Glasgow, United Kingdom, Mar. 2024, pp. 1–5.
- [26] Y. Zhu, A. Vilenskiy, O. Iupikov, P. Krasov, T. Emanuelsson, G. Lasser, and M. Ivashina, "Improved equivalent circuit model of p - i - n diodes for amplitude and phase controllable mmWave reconfigurable intelligent surfaces," in *Proc. IEEE Int. Symp. Antennas Propag. INC/USNC-URSI Radio Sci. Meeting (AP-S/INC-USNC-URSI)*, Firenze, Italy, Jul. 2024, pp. 1583–1584.
- [27] J.-M. Baracco, P. Ratajczak, P. Brachat, J.-M. Fargeas, and G. Toso, "Ka-band reconfigurable reflectarrays using varactor technology for space applications: A proposed design," *IEEE Antennas Propag. Mag.*, vol. 64, no. 1, pp. 27–38, Feb. 2022.
- [28] R. Wang, Y. Yang, B. Makki, and A. Shamim, "A wideband reconfigurable intelligent surface for 5G millimeter-wave applications," *IEEE Trans. Antennas Propag.*, vol. 72, no. 3, pp. 2399–2410, Mar. 2024.
- [29] E. Wang, G. Peng, K. Zhong, F. Wu, Z. H. Jiang, R. Sauleau, and W. Hong, "A 1296-cell reconfigurable reflect-array antenna with 2-bit phase resolution for Ka-band applications," *IEEE Trans. Antennas Propag.*, vol. 72, no. 4, pp. 3425–3437, Apr. 2024.
- [30] A. Araghi, M. Khalily, M. Safaei, A. Bagheri, V. Singh, F. Wang, and R. Tafazolli, "Reconfigurable intelligent surface (RIS) in the sub-6 GHz band: Design, implementation, and real-world demonstration," *IEEE Access*, vol. 10, pp. 2646–2655, 2022.
- [31] J. C. Liang, Q. Cheng, Y. Gao, C. Xiao, S. Gao, L. Zhang, S. Jin, and T. J. Cui, "An angle-insensitive 3-bit reconfigurable intelligent surface," *IEEE Trans. Antennas Propag.*, vol. 70, no. 10, pp. 8798–8808, Oct. 2022.
- [32] S. Zeng, H. Zhang, B. Di, Y. Liu, M. Di Renzo, Z. Han, H. V. Poor, and L. Song, "Intelligent omni-surfaces: Reflection-refraction circuit model, full-dimensional beamforming, and system implementation," *IEEE Trans. Commun.*, vol. 70, no. 11, pp. 7711–7727, Nov. 2022.
- [33] S. V. Hum and B. Du, "Equivalent circuit modeling for reflectarrays using floquet modal expansion," *IEEE Trans. Antennas Propag.*, vol. 65, no. 3, pp. 1131–1140, Mar. 2017.
- [34] E. Baladi and S. V. Hum, "Equivalent circuit models for metasurfaces using floquet modal expansion of surface current distributions," *IEEE Trans. Antennas Propag.*, vol. 69, no. 9, pp. 5691–5703, Sep. 2021.
- [35] M. Pérez-Escribano, S. Moreno-Rodríguez, C. Molero, J. F. Valenzuela-Valdés, P. Padilla, and A. Alex-Amor, "Analytical framework to model reconfigurable metasurfaces including lumped elements," *IEEE Trans. Circuits Syst. II, Exp. Briefs*, vol. 71, no. 4, pp. 1784–1788, Apr. 2024.
- [36] R. J. Chaffin, "Permanent neutron damage in PIN microwave diode switches," *IEEE Trans. Nucl. Sci.*, vol. 18, no. 6, pp. 429–435, Dec. 1971.
- [37] A. K. Bhattacharyya, "Floquet modal functions," in *Phased Array Antennas: Floquet Analysis, Synthesis, BFNs and Active Array Systems*. Hoboken, NJ, USA: Wiley, 2006, pp. 89–128.
- [38] D. Schaubert, F. Farrar, A. Sindoris, and S. Hayes, "Microstrip antennas with frequency agility and polarization diversity," *IEEE Trans. Antennas Propag.*, vol. 29, no. 1, pp. 118–123, Jan. 1981.

- [39] C. R. Paul, "Loop inductance vs. partial inductance," in *Inductance: Loop and Partial*. Hoboken, NJ, USA: Wiley, 2010, pp. 307–333.
- [40] T. C. Edwards and M. B. Steer, "Discontinuities in microstrip," in *Foundations for Microstrip Circuit Design*, 4th ed. Hoboken, NJ, USA: Wiley, 2016, pp. 227–267.
- [41] D. M. Pozar, "Transmission line theory," in *Microwave Engineering*, 4th ed. Hoboken, NJ, USA: Wiley, 2011, pp. 48–94.
- [42] P. Nayeri, F. Yang, and A. Z. Elsherbeni, "Analysis and design of reflectarray element," in *Reflectarray Antennas: Theory, Designs, and Applications*. Hoboken, NJ, USA: Wiley, 2018, pp. 9–48.
- [43] A. F. Vaquero, R. Florencio, M. R. Pino, and M. Arrebola, "Dual-polarized near-field plane wave generator using an offset-optics reflectarray mm-wave band," *IEEE Trans. Antennas Propag.*, vol. 70, no. 12, pp. 12370–12375, Dec. 2022.
- [44] J. Tang, X. Chen, X. Meng, Z. Wang, Y. Ren, C. Pan, X. Huang, M. Li, and A. A. Kishk, "Compact antenna test range using very small F/D transmitarray based on amplitude modification and phase modulation," *IEEE Trans. Instrum. Meas.*, vol. 71, pp. 1–14, Art no. 8001614, Feb. 2022.
- [45] O. A. Iupikov, P. S. Krasov, A. A. Glazunov, R. Maaskant, J. Fridén, and M. V. Ivashina, "Hybrid OTA chamber for multidirectional testing of wireless devices: Plane wave spectrum generator design and experimental demonstration," *IEEE Trans. Antennas Propag.*, vol. 70, no. 11, pp. 10974–10987, Nov. 2022.
- [46] 3GPP, "Release 15 description; Summary of Rel-15 work items," Tech. Rep. 21.915, V15.0.0, Sep. 2019.



Yuqing Zhu (S'18) received the B.S. degree in electronic information engineering and the M.S. degree in electronics science and technology from Beijing Institute of Technology, Beijing, China, in 2019 and 2022, respectively.

He is currently pursuing the Ph.D. degree with the Antenna Systems Group, Department of Electrical Engineering, Chalmers University of Technology, Gothenburg, Sweden. His current research interests include millimeter-wave antennas and arrays, phased array antennas, 5G/6G mobile terminal antennas, reconfigurable intelligent surfaces, and over-the-air testing techniques.

Mr. Zhu was a recipient of the Oral Best Paper Award at ICEICT 2020, the Best Student Paper Award at ICMMT 2022, the Student Travel Grant from the IEEE Antennas and Propagation Society at AP-S/INC-USNC-URSI 2024, and the Master's Thesis Incentive Program from the Chinese Institute of Electronics in 2024. He serves as a reviewer for several academic publications, including IEEE TRANSACTIONS ON ANTENNAS AND PROPAGATION, IEEE ANTENNAS AND WIRELESS PROPAGATION LETTERS, *IET Microwaves, Antennas & Propagation*, and *Electronics Letters*.



Artem R. Vilenskiy (M'11–SM'24) received the specialist degree (*summa cum laude*) in radioengineering and the Ph.D. degree in antennas and microwave devices from Bauman Moscow State Technical University, Moscow, Russia, in 2011 and 2014, respectively.

From 2011 to 2019, he was with Samsung Research Institute Russia, Moscow, Russia, where he had roles of researcher, expert engineer, and project leader in Electromagnetics Group and RF Sensor Part. From 2015 to 2019, he was an Associate

Professor at the Radio-Electronic Systems and Devices Department of Bauman Moscow State Technical University. In 2019–2024, he was a Researcher with Antenna Systems Group, Chalmers University of Technology, Gothenburg, Sweden. He is currently a Microwave Team Lead at Xpanceo, Dubai, UAE. His research interests include applied and computational electromagnetics, antenna and front end integrated circuit design, controllable high-frequency materials and devices.



Oleg A. Iupikov (S'12–M'19) received a M.Sc. degree (*cum laude*) in electrical engineering in 2006, from the Sevastopol National Technical University, Ukraine. After graduating, he was working at the Radio Engineering Bureau, Sevastopol. During this period, he was also a visiting researcher at the Netherlands Institute for Radio Astronomy (ASTRON), where he was involved in the development of the focal plane array simulation software for the APERTIF radio telescope. Oleg received his Ph.D. degree from the Chalmers University of Technology

(Gothenburg, Sweden) in 2017 and currently works there as a researcher.

His research interests are receiving array antenna systems, in particular focal plane arrays for radio astronomy and microwave remote sensing applications, numerical methods for their analysis and optimization, signal processing algorithms for antenna systems, integration of antennas with active components, and OTA characterization of active and passive devices.



Pavlo S. Krasov (Member, IEEE) received the B.Sc. and M.Sc. degrees in physical sciences from V. N. Karazin Kharkiv National University, Kharkiv, Ukraine, in 2002 and 2003, respectively, and the Ph.D. degree in physics of devices, components, and systems from the Kharkiv National University of Radioelectronics, Kharkiv, in 2012.

Since 2008, he has been a Research Fellow with the Institute of Radiophysics and Electronics National Academy of Science (NAS) of Ukraine, Kharkiv, where he was involved in millimeter-wave

and electrical engineering in biomedical applications. In 2019, he joined the Antenna Group at the Chalmers University of Technology, Gothenburg, Sweden, where he started his work as a Research Scientist. His current research interests include antennas and array antennas, antenna measurement sites, over-the-air characterization techniques and hardware implementations, and 3-D printing applications in antennas.



Thomas Emanuelsson received the M.S. degree in electronic engineering from Chalmers University of Technology, Gothenburg, Sweden, in 1984.

He is currently holding a position as a Senior Expert in microwave and sub-THz technology at Ericsson AB, and also a position as an Adjunct Professor at the Microwave Electronics Laboratory, Department of Microtechnology and Nanoscience (MC2), Chalmers University of Technology. He has extensive background in mmWave radio communication, radar phased array systems, and monolithic

microwave integrated circuit (MMIC) technology.



Gregor Lasser (Senior Member, IEEE) is an Assistant Professor with Chalmers University of Technology. He received the Dipl.-Ing. and Dr. Techn. degrees in electrical engineering (both with distinction) from Vienna University of Technology, Vienna, Austria, in 2008 and 2014, respectively. From 2016 to 2021, he served as the Vice Chair of the IEEE Denver joint AP-S/MTT section. In 2015, he joined the University of Colorado, Boulder, from August 2017 until December 2022 as an Assistant Research Professor.

Dr. Lasser's research interests are in broadband supply and bias modulated power amplifiers, analog linearization, electronically augmented antennas, and active interference cancellation circuits. His research so far has received several prizes, starting with the second prize EEEfCOM innovation award in 2008 for his diploma thesis project. His doctoral dissertation on passive RFIDs for automotive sensors received the department award of the electrical engineering and information technology department of the Vienna University of Technology. In April 2017, he received the best paper award of the WAMICON conference.



Marianna V. Ivashina (M'11–SM'13) received a Ph.D. in electrical engineering from the Sevastopol National Technical University (SNTU), Ukraine, in 2001. From 2001 to 2010 she was with the Netherlands Institute for Radio Astronomy (ASTRON), where she carried out research on innovative phased array technologies for future radio telescopes, such as the Square Kilometer Array. In 2002–2003, she also stayed as a Visiting Scientist with the European Space Agency, ESTEC, where she studied multiple-beam array feeds for the satellite telecommunication

system Large Deployable Antenna.

In January 2011, she joined Chalmers University of Technology (Gothenburg, Sweden), where she is currently a Full Professor and the Head of the Antenna Systems Group at the Department of Electrical Engineering. Her current research interests include antenna array systems, integration of antennas with active electronic components, synthesis of aperiodic arrays, and other unconventional array architectures, reflector antennas, and focal plane array feeds. She has published extensively on the above topics, having authored/co-authored over 130 journal and conference papers. She has received several scientific awards [including the URSI Young Scientists Award for GA URSI, Toronto, Canada (1999), the APS/IEEE Travel Grant, Davos, Switzerland (2000), the "Best team contribution" Paper Award at the ESA Antenna Workshop (2008), the EU FP7 Marie Curie Actions International Qualification Fellowship (2009), the Best Paper Award at the IEEE COMCAS Conf., Tel-Aviv, Israel (2019)], and numerous research project funding grants from Swedish and European funding agencies.

Prof. Ivashina was previously an Associate Editor of the IEEE TRANSACTIONS ON ANTENNAS AND PROPAGATION and is currently a Board Member of the European School of Antennas (ESoA). Since 2021, she has been the Delegate of the European Association of Antennas and Propagation (EurAAP) for Region 6: Iceland, Norway, and Sweden.